A COMPUTER VISION BASED METHOD FOR SEMI-AUTOMATED REBAR DETECTION AND MEASUREMENT OF REINFORCED CONCRETE COLUMNS

A THESIS SUBMITTED TO
THE GRADUATE SCHOOL OF NATURAL AND APPLIED SCIENCES
OF
MIDDLE EAST TECHNICAL UNIVERSITY

BY
MUHAMMAD USMAN HASSAN

IN PARTIAL FULFILLMENT OF THE REQUIREMENTS
FOR
THE DEGREE OF MASTERS OF SCIENCE
IN
CIVIL ENGINEERING

SEPTEMBER 2014

Approval of the thesis:

A COMPUTER VISION BASED METHOD FOR SEMI-AUTOMATED REBAR DETECTION AND MEASUREMENT OF REINFORCED CONCRETE COLUMNS

Submitted by **MUHAMMAD USMAN HASSAN** in partial fulfillment of the requirements for the degree of Masters of Science in **Civil Engineering Department, Middle East Technical University** by,

Prof. Dr. Canan Özgen ______________________
Dean, **Graduate School of Natural and Applied Sciences**

Prof. Dr. Ahmet C. Yalçıner ______________________
Head of Department, **Civil Engineering**

Assoc. Prof. Dr. Özgür Kurç ______________________
Supervisor, **Civil Engineering Dept., METU**

Examining Committee Members:

Asst. Prof. Onur Pekcan ______________________
Civil Engineering Dept., METU

Assoc. Prof. Dr. Özgür Kurç ______________________
Civil Engineering Dept., METU

Assoc. Prof. Dr. Ahmet Türer ______________________
Civil Engineering Dept., METU

Asst. Prof. Dr. Aslı Akçamete ______________________
Civil Engineering Dept., METU

Assoc. Prof. Dr. Demirkan Çoker ______________________
Aerospace Engineering Dept., METU

Date : 1st -September-2014

I hereby declare that all information in this document has been obtained and presented in accordance with academic rules and ethical conduct. I also declare that, as required by these rules and conduct, I have fully cited and referenced all material and results that are not original to this work.

Name, Last name : Muhammad Usman, Hassan

Signature :

ABSTRACT

A COMPUTER VISION BASED METHOD FOR SEMI-AUTOMATED REBAR DETECTION AND MEASUREMENT OF REINFORCED CONCRETE COLUMNS

Muhammad Usman Hassan

MS, Department of Civil Engineering

Supervisor: Assoc. Prof. Dr. Özgür Kurç

September 2014, 94 Pages

As-built information of reinforced sections is necessary to ascertain structural characteristics from load carrying capacity, serviceability, structural integrity and adherence to code perspective. The objective of this research is to develop a semi-automated structural information acquisition method that can be used to determine as-built information regarding rebar grids of reinforced concrete columns. The technique involves application of photogrammetry, image processing and computer vision knowledge to obtain structural information in 2D and 3D space. Method developed during the course of this research is divided into bar detection, bar diameter measurement, stirrup spacing, and 3D rebar location computation algorithms. Multi prong approach of color space and line detection is utilized to add robustness to the method. In order to improve automation of developed product a stereo matching algorithm is developed to match points between two images of symmetric and hollow rebar grids. Every step of the proposed method is tested on different rebar specimens with varying dimensions and complexity to adjudge its performance. Based on images acquired in ideal condition, the error in measurement of rebars diameters and stirrup spacing remained below 8.5%. For 3D measurement of rebar coordinates, error has increased up to 20%.

Key Words; Image Processing, Automation

ÖZ

BETONARME KOLONLAR İÇİN SAYISAL GÖRÜNTÜ İŞLEME TEMELLİ YARI OTOMATİK DONATI ÖLÇME VE BELİRLEME YÖNTEMİ

Muhammad Usman Hassan
Yüksek Lısans, İnşaat Mühendisliği Bölümü
Tez Yöneticisi: Doç. Dr. Özgür Kurç
Eylül 2014, 94 safya

Betonarme kesitlerin imal ediliş şekliyle ilgili bilgiler, yapısal tasarım kodu temelli yük taşıma kapasitesi, kullanılabilirlik kriterleri ve yapısal bütünlük gerekliliklerine uyumluluğun tespit edilebilmesi için gereklidir. Bu çalışmanın da amacı, betonarme kolonların donatı örgüsünün özellikleri belirlenmesini sağlayan yarı otomatik bir yöntem geliştirmektir. Geliştirilen yöntem, fotogrametri, görüntü işleme ve bilgisayar görüşü tekniklerinin iki ve üç boyutta yapısal bilgi edinme için kullanılmasını içermektedir. Çalışma kapsamında geliştirilen yöntemin ana aşamaları donatıların belirlenmesi, donatı çapı ve etriye aralıklarının ölçümü ve üç boyutta donatıların koordinatlarının belirlenmesidir. Renk alanının ve kenar belirleme yöntemlerinin kullanılması geliştirilen algoritmaların esnekliğini arttırmıştır. Geliştirilen yöntemin otomatikliğini arttırmak amacıyla farklı bir stereo eşleştirme algoritması da geliştirilmiştir. Bu yeni algoritmayla iki farklı açılardan çekilmiş fotoğraflarda, simetrik ve boşluklu donatı örgüsündeki aynı noktaların tespiti otomatikleştirilmiştir. Geliştirilen yöntemin her bir aşaması, farklı donatı sayısına ve aralıklarına sahip numuneler üzerinde sınanmıştır. Elde edilen sonuçlara göre ideal koşullarda çekilen fotoğraflardan yapılan donatı çapı ve etriye aralığı ölçümlerinde görülen hata payı 8.5'in altında kalmıştır. Donatı koordinatlarının belirlenmesinde hata payı 20'e kadar çıkmıştır.

Anahtar kelimeler; Görüntü işleme, otomasyon

To,

The People of my country and their countless sacrifices

&

My Parents

&

My wife Sara and my son Ammar

ACKNOWLEDGEMENTS

I am grateful to my supervisor Dr. Ozgur Kurc for his mentorship; guidance and continuous support that made research in such an innovative and completely new field a possibility. I am grateful to MIT, Stanford, Colorado School of Mines, Khan Academy and William Hoffman for open courseware material that was very useful throughout the course of the thesis.

I am grateful to Dr. Onur Pekcan, Dr. Asli Akçamate, Dr. Demirkan Çoker and Dr. Ahmet Türer for very useful feedback that helped me improve my thesis document a lot. I am extremely grateful to my father for careful proof reading of the thesis material, my mother for her love and prayers, my wife for bearing with me and my long hours of study during the course of this work. I feel for my son, who has been ignored inorder to achieve the objective of this study.

I am grateful to HEC for financial support for the MS and PhD and METU Structural Engineering Department for provision of all kind of support that was required.

TABLE OF CONTENTS

LIST OF TABLES

LIST OF FIGURES

CHAPTER 1

INTRODUCTION

With the decreasing cost of computing and image acquisition hardware, cutting edge technology in the field of vision is becoming more and more accessible to construction professionals. Although construction industry is considered to be a traditional field which focuses on heavy engineering and labor intensive work, yet it has also begun to benefit from automation and robotics which includes application of vision technologies as well.

As the world progresses into the information systems, there is more need for automation and use of cutting edge technology in order to keep development sustainable and financially viable. The resource scarcity is making it more important for architects, engineers and construction (AEC) communities to manage resources efficiently (Ali et al., 2012). This is the reason that, in the past few decades, there has been a growing interest in BIM due to many benefits of resource saving during design, planning and construction phases of new buildings (Leite et al., 2011).

Application of computer vision techniques in civil engineering is useful for construction quality inspection and progress monitoring purposes which, to date have been manual labor intensive processes prone to human error. Construction quality assurance is specifically a critical area in the field of construction management. Optimum quality is attained by physical inspection at every step of construction making sure that all dimensions and constraints are kept in mind. According to Akinci et al., 2006, current approaches of quality control on construction sites are not as effective as they could be, in identifying defects early in construction process. The observations from the checklists filled by inspectors are evaluated resulting in non-conformities and observations that become part of the Total Quality Management

Process (TQM) documentation. Construction is critical and tricky task which involves large amounts of human and environmental variables that tend to affect longitudinal rebars, stirrups spacing and reduce structural capacity of the concrete columns.

Photogrammetry and computer vision were developed initially to serve the military purposes, however, with the passage of time, vision applications have found utility in all kinds of engineering and medical applications. In the construction industry, the application of computer vision is for deviation detection (Klein, Li, & Becerik-Gerber, 2012), as built modeling (Brilakis, Fathi, & Rashidi, 2011), structural health monitoring (Olsen, Kuester, Chang, & Hutchinson, 2010), automated progress monitoring (Dimitrov & Golparvar-Fard, 2014) and record updates (Shih, Wu, & Kunz, 2004) etc. The use of LIDAR scanner or Optical Cameras is customary for above mentioned applications. Both techniques have a set of advantages and disadvantages from cost and computational perspectives. The need remains of digitized as-built information that can be used throughout the life cycle of the project, whenever need arises.

Computer vision has found its application in project management (Abeid et al., 2003), construction progress monitoring (Roh, Aziz, & Peña-Mora, 2011), construction safety assurance, and equipment tracking. These are usually used in conjunction with sensors for construction automation applications.

RC members are usually cast in situ and all workmanship is performed on site. The lack of education among construction labor, coupled with space constraint and workmanship factors creates deviation from structural drawings without any consent from the consultants. Construction quality assurance is very important from structural engineering perspective, as defects during construction severely affect the structural characteristics of the structure. These defects include use of wrong diameter bars and improper spacing between vertical rebar elements and horizontal stirrups. Spacing between rebars should be as accurate as possible, since too high spacing or too less spacing are both detrimental to structural integrity of the structure. These considerations become extremely important when construction is being done in adherence to the earth quake code in an earth quake prone area. Many structural deficiencies were highlighted as the cause of earthquake damage that included reinforcement with insufficient confinement and transverse reinforcement during a study of performance of reinforced buildings during Kocaeli Earthquake (Sezen, Whittaker, Elwood, & Mosalam, 2003)

Structural As-built information remains very important throughout the life cycle of a structure. As-built information is used to confirm compliance to code and location regulations as well as a measure to confirm serviceability after a disaster like earth quake or explosion etc. Structural information comes into play when structures are being expanded or demolished. Engineers can't rely on structural design and shop drawings since the dimensions and spacing change during construction work due to various issues. Structural Quality Assurance is a tedious task and requires considerable amount of man-hours and physical effort. All inspections are done physically by inspectors; there is considerable likelihood of human error and over sight. Also, it is not possible for inspectors to be present at all locations at all times consequently, there is always room for error. If the process of quality assurance is automated, the above mentioned drawbacks of physical inspection can be offset. There would be no particular need to fill the checklists and manually update the quality record; rather all information could be automatically distributed to the responsible personnel. Structural strength of RC members can be severely compromised by violation of drawings and specifications. The longitudinal rebars and stirrup spacing requirement ensure workability and avoids honey combing. The plastic hinge regions are extremely critical in performance of structure during dynamic loading like earthquake. Improper stirrup spacing can cause failure at critical section causing complete collapse or rendering the structure completely unserviceable.

1.1. Literature Review

Less amount of work has been done on application of computer vision in the field of construction. Two types of vision applications exist in research. One is based on active equipment like Laser scanner while others are based on passive equipment like cameras. Combinations of laser scanner and cameras have also been utilized in research in some instances.

Acquisition of construction information can be achieved either by a 3D Laser scanner commonly referred to as Light Detection And Ranging (LIDAR) which is a measurement instrument that uses line of sight to measure distances from the objects. Laser scanner can acquire large amount of information in a short period of time by using various commercially available software. This information can be converted into point's cloud and information related to model geometry can be extracted. However, laser scanners are greatly affected by environmental and physical conditions such as large windows and glazing. The movement of targets also tends to add inaccuracies to the information acquired. Laser scanner also tends to be inaccurate when there are sharp corners and edges. The main issues with laser scanners are very high cost and high level of skill and training required by the users (Klein et al., 2012). However because of accuracy provided by laser scanners, LIDAR scanners have found considerable use in structural information acquisition. Terrestrial laser scanning data is suggested for structural damage assessment by volumetric and damage detection analysis for a full scale structural specimen (Olsen et al., 2010). The laser data can also be used for progress monitoring by Boolean operation of point clouds that provides a theoretical foundation of algorithmic calculation of as-built processes (Shih et al., 2004).

Gated imaging is a technique that combines the benefits of imaging through cameras and pulse generating laser. Gated imaging system involves obtaining images of objects only from a certain distance which makes it easier to differentiate between important object and irrelevant background (Śluzek, 2010).

Photogrammetry and computer vision are used interchangeably basically encapsulating the technique of attaining shape information of any object by processing its images instead of measuring it directly. If the distance of image from the sensor is more than 100m then this technique is called close range photogrammetry. Based on information about mechanics and physical characteristics of imaging systems, mathematical models are devised which are the basis of numerical method used for attaining coordinate information about discrete points on an image. Photogrammetry is a science and involves use of mathematical relations a lot but, at the same time, it is considered an art therefore requiring skill and foresight from the person taking images. The knowledge of the scene and the requisite information play an important role in image acquisition techniques based on the problem at hand. Stereo matching algorithms like Segment-Tree based Cost Aggregation for Stereo Matching (Mei et al., 2013) have been suggested for non-local matching cost aggregation. The process consists of three steps where pixels are grouped in a set of segments followed by tree graph creation thus forming independent segment tree structures. The use of epipolar lines to perform stereo matching for un calibrated cameras (Zhang et al., 1994) perform stereo matching while camera positions are unknown, afterwards Least Median of Square Estimates (LMedS) to discard outliers. For stereo matching, the methods are either local or global such as adaptable windows (Yoon & Kweon, 2005) or global like graph cuts (Kolmogorov & Zabih, 2001). Graph cuts can be used for dense stereo matching using color segmentation on the reference image (Bleyer & Gelautz, 2007). The algorithm is capable of handling large un-textured objects which are difficult to handle by conventional stereo matching techniques as mentioned by the author in the same study. Photogrammetric techniques have been applied from crack width monitoring to bridge deflection measurement and beam deflections in load tests as well as long term deflections in reservoirs (Mass & Hampel, 2006).

Computer vision is applied to construction management mostly for inspection and monitoring purposes. The inspection application is related to crack monitoring (Sohn, Lim, Yun, & Kim, 2005) and bridge inspection (Abudayyeh, Al Bataineh, & Abdel-Qader, 2004) etc. The objective of this research is either to detect various anomalies and defects or find metric information for as-built modeling and measurement purposes. The color information along with edge detection and segmentation algorithms is used for object recognition and to differentiate the structure from its surroundings. The color information is based on thresholding of HSI values to obtain location of respective elements. This requires training of algorithm on a series of training and testing data and has also been used for progress monitoring in steel structures (Son & Kim, 2010).

Research work has been done on implementation of construction information technology in the construction industry. The most relevant article is related to use of image processing for 3D reconstruction (Brilakis et al., 2011). 3D reconstruction is achieved using images extracted from videos. The technique uses videogrammetry for 3D reconstruction and creation of point cloud. The proposed framework involves videogrammetry using a calibrated set of stereo cameras. The paper recommends Speeded-up Robust Feature (SURF) which is a scale and rotation invariant feature detector and descriptor. In the next step there is structure and motion recovery which involves recovery of 3D coordinates of the scene and motion information of cameras between two successive frames. The structure of the scene is calculated using simple triangulation. Sparse 3D point cloud can also be generated by the use of photographs on the basis of distinctive visual features (Fathi & Brilakis, 2011). Sparse 3D cloud in comparison with dense 3D cloud is computationally less expensive.

The worksite spatial data obtained through use of image processing can assist contractors and workers in controlling various aspects of an infrastructure project (Gordon et al., 2003), spatial data acquisition (Akinci et al., 2002) and monitoring construction progress in a proactive manner (Shih et al., 2004). As-built information can also help designers in assessing deviation from their design and operators in monitoring its deflection deterioration (Olsen et al., 2010).

1.2. Objectives and Scope

Objectives of this study are as follows;-

1. To develop a method for rebar detection and 2D measurement of rebar column elements from acquired images.
2. To extract 3D information of reinforced concrete column rebar coordinates from acquired images.

The scope of the study is limited to reinforced concrete columns with all rebars vertical and of the same diameter. The scope is limited to detection, measurement and 3D coordinate determination of rebars, followed by plot of the rebar column. The purpose is to acquire correct information of rebar spacing and diameter to adjudge compliance of the structure with the requirement of earthquake and concrete codes. The actual information can then be used in future expansion, repair and quality assurance applications. The study is conducted on concrete columns only thus excluding beams, footings and shell elements.

The thesis consists of 5 Chapters, 1^{st} chapter provides introduction, 2^{nd} chapter gives background information about details of image processing and computer vision. The 3^{rd} chapter explains the method and algorithms within the method. The 4^{th} chapter is related to results of application of method while the 5^{th} chapter concludes the study.

CHAPTER 2

BACKGROUND INFORMATION

2.1. Introduction

Structural As-built information of concrete members holds prime importance throughout the lifecycle of a project. This information is required in case the structural load carrying capacity needs to be evaluated or serviceability has to be determined after a major earthquake. Structural As-built information is required whenever a structure is being modified or demolished. An automated structural information acquisition method is developed by the use of photogrammetry, image processing and computer vision. The subject knowledge areas are discussed and utilized in order to achieve the objectives of this research.

Various intricacies related to photogrammetry, image processing and computer vision knowledge areas need to be understood before development of a comprehensive method. The geometry of camera forms the building block of 3D objects transformation to 2D image on an image plane. The camera matrix is inherent part of the 3D vision that is determined by camera calibration experiment. The fundamental matrix computation and derivation becomes building block of all 3D vision processes. The basics of image processing including filtering and edge detection algorithms are required to enhance images for application of algorithm. Line detection is applied to detect and plot rebars and color thresholding information, which forms the basis of various algorithms that are part of automated method developed during this research. The purpose of this chapter is to provide brief insight into world of vision.

2.2. Photogrammetry

Photogrammetry is the process of obtaining position, size and shape of an object by measuring image of object rather than the object itself (Fryer, 2001). In close range photogrammetric, the extent of object to be measured is less than 100m and cameras are pointed close to the object. Camera axes are usually parallel in certain cases and in most cases they are highly convergent pointing in the same direction. Mathematical models are created, based on understanding of processes of image acquisitions in order to form basis of various numerical methods to produce three-dimensional coordinates of discrete points on an object. Machine learning algorithms and concepts are utilized in photogrammetric processes to extract desired information from image. Results of imaging are easily and instantaneously available, making it easy to process and extract the required information in the form of measurements.

2.2.1. Coordinates and Coordinates Transformations

Coordinate transformations from a local to global coordinate system are defined by a three dimensional Cartesian coordinate system which includes the origin, the scale and the orientation which can be arbitrarily defined. The coordinates of the object and the camera in a secondary (*xy)* system have to be transformed into global coordinates (X, Y) using transformation and translation matrix. A commonly used transformation is called *bilinear transformation* given by Equation. 2.1

$$\begin{aligned} X &= a_0 + a_1 x + a_2 y + a_3 xy \\ Y &= b_0 \ + \ b_1 x + b_2 x + \ b_3 xy \end{aligned} \qquad \textbf{(2.1)}$$

2.3. Camera Geometry

The most important aspect of a photogrammetry is central perspective projection. A specific point is projected onto a projection screen by a straight line. Referring to Figure 2.1, the perspective axis *'Pop'* is orthogonal to the projection plane which it intersects at *p*, the principal point. The distance *OP* is called the principal distance usually denoted by c. The two points on '*A'* and 'a' are homologous points.

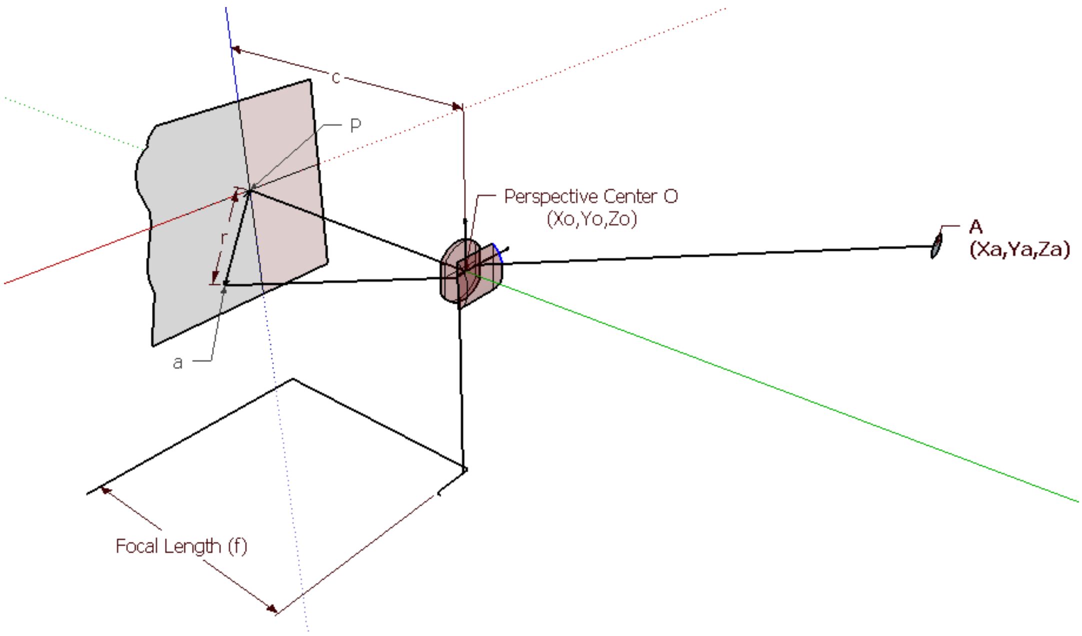

Figure 2.1 Representation of Camera Geometry.

If we assume two Cartesian coordinate systems, the primary and the secondary coordinate systems, the primary system (XYZ) is located arbitrarily in object space while the secondary coordinate system (xyz) has its origin at the perspective center and its z axis coincides with the principal axis. The coordinates of image projection are given by (x,y,-c). Vector written w.r.t Primary coordinates system is given by Equation 2.2

$$\underline{\boldsymbol{X_A}} = \underline{\boldsymbol{X_0}} - \boldsymbol{\mu}\underline{\boldsymbol{R^t}} \tag{2.2}$$

This can be written as following notation given by Equation 2.3

$$\begin{vmatrix} X_A \\ Y_A \\ Z_A \end{vmatrix} = \begin{vmatrix} X_0 \\ Y_0 \\ Z_0 \end{vmatrix} + \begin{vmatrix} r_{11} & r_{21} & r_{31} \\ r_{12} & r_{22} & r_{32} \\ r_{31} & r_{32} & r_{33} \end{vmatrix} . \begin{vmatrix} x_a \\ y_a \\ -c \end{vmatrix} \tag{2.3}$$

2.4. Camera Parameters

Camera has both intrinsic parameters that are independent of location and orientation of camera, and extrinsic matrix that are based on location and orientation of camera. Camera parameters are given in the following sections,

2.4.1. Intrinsic Parameters

Camera intrinsic parameters are independent of the location and pose of the camera, therefore they remain constant throughout the duration of the experiment until or unless the zoom of the camera is altered. The best option is to use a non-zoom lens with and focus fixed at infinity and all kinds of sharpening and image improvement processes turned off for best results.

2.4.1.1. Focal Length

Focal length is usually measured in mm and depicts how strongly a lens converges light. For a thin air lens, focal length is the distance from lens to the principal foci. The lesser the focal length the greater the optical power of the lens and greater the angle of view.

2.4.1.2. F-Number

F number is the ratio of the aperture and focal length given by the relation in Equation 2.4

$$N = \frac{f}{D} \tag{2.4}$$

Where f is the focal length and D is the diameter of the entrance of pupil.

2.4.1.3. Location of Principal Point

The x and y coordinates of principal point are also fixed parameter of the camera represented in pixel. If this parameter is not known, the center of CCD sensor is considered to be the principal point.

2.4.1.4. Radial and Tangential Distortion of Lens

Variation of angular magnifications are usually interpreted as radial lens distortion (Fryer, 2001). Radial distortion is a function of radial distance from the point of symmetry and expressed as a polynomial given by the relation in Equation 2.5.

$$\delta r_x = K_1 r^3 + K_2 r^5 + \ K_3 r^7 \tag{2.5}$$

Where δr is the radial displacement of image point, $r^2 = (x-x_0)^2+(y-y_0)^2$, (x, y) are fucidial coordinates of the point of symmetry or principal axis. The value of constants depends upon camera focal settings.

Tangential distortion of lens is the displacement of a point in an image caused by misalignment of cells and is described by polynomials whose coefficients depend upon camera focal length setting.

2.4.1.5. Camera Calibration Matrix

Camera calibration matrix provides the intrinsic parameters and is given by the Equation 2.6.

$$K = \begin{bmatrix} \alpha_x & 0 & t_x \\ 0 & \alpha_y & t_y \\ 0 & 0 & 1 \end{bmatrix} \tag{2.6}$$

The elements of camera intrinsic matrix contain focal length (α_x, α_y) information in terms of pixels and principal point $(t_x t_y)$information as well. The camera instrinsic matrix can be estimated on the basis of Exchange Image File Format data but the estimation would not be accurate, therefore, calibration is required in order to estimate correct parameters.

2.5. Camera Calibration

Camera calibration can be done using the Photo modeler Pro software (Eos Systems Inc, 2014) as well as Calibration toolbox for Matlab (Bouguet, 2013). Both programs are easy to use and provide consistent results. Calibration can be either multi-sheet or single sheet calibration depending upon the application. **Figure 2.2** shows calibration grid for Matlab used for experiment.

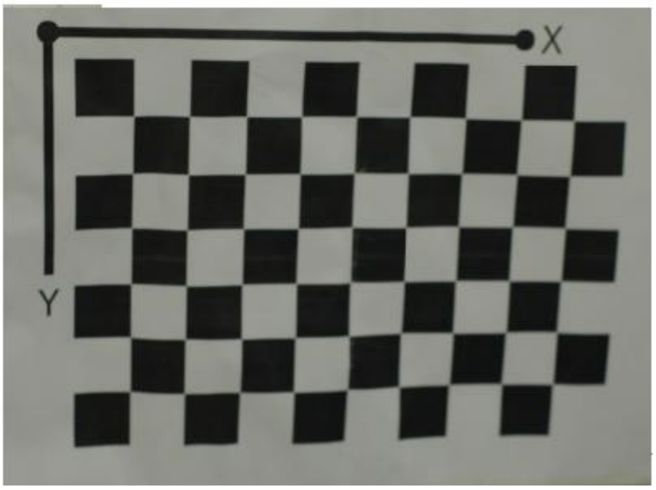

Figure 2.2 Camera Calibration checkerboard from Matlab Calibration Toolbox

The images are calibrated and results are stored as camera calibration parameters in the memory to be used in future for 3D reconstruction.

2.5.1. Camera Extrinsic Parameters

Camera extrinsic parameters are dependent on the pose of the camera relevant to the world coordinate system. They are reflected in terms of camera rotation and translation matrices from the global coordinate axis origin. The camera extrinsic parameters can be measured from translation and rotation of known world coordinate points and the relation of camera coordinates w.r.t world coordinates is given by Equation 2.7. In Equation 2.7, $X_{c,}$ $Y_{c,}$ Z_c represent the object coordinates in camera coordinate system while X, Y, Z represent object coordinates in world coordinate system.

$$\begin{bmatrix} X_C \\ Y_C \\ Z_C \\ 1 \end{bmatrix} = K[R|t] \begin{bmatrix} X \\ Y \\ Z \\ 1 \end{bmatrix} \tag{2.7}$$

Camera extrinsic and intrinsic parameters combine to form the camera matrix that would change once camera is moved from its location. Thus camera matrix for location ‘1’ is given by the following relation shown in Equation 2.8.

$$P_i = K_i[R_i|t_i] \tag{2.8}$$

2.5.1.1. Calculation of Camera Extrinsic Parameters

Extrinsic camera parameters are calculated by taking one camera as a reference. The extrinsic matrix for the reference camera is given by Equation 2.9.

$$P_1 = \underline{K}\left[\underline{I}\middle|0\right] \tag{2.9}$$

Where K is the camera calibration matrix and I is the identity matrix. The poise of the remaining camera P_i is given by the translation and rotation of R_i and translation vector ti. Therefore the camera calibration matrix is given by relation in Equation 2.10.

$$P_i = \underline{K}\left[\underline{\boldsymbol{R_i}}\middle|\tilde{t}\right] \tag{2.10}$$

The camera matrix can be computed using the singular value decomposition of fundamental matrix. The extrinsic parameters are also calculated by using the calibration toolbox for Matlab. The printed checkerboard is kept within frame of the camera and corners are manually defined on the calibration grid.

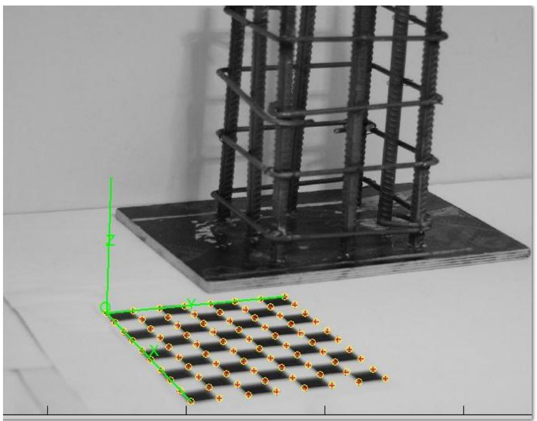

Figure 2.3 Camera Extrinsic Coordinate System with respect to Calibration Grid.

The toolbox calculates the extrinsic camera matrix based on world coordinate system whose origin is located on the top left corner of checkerboard. Figure 2.3 shows world camera coordinate axis orientation on the checkerboard plane.

2.6. Choice of Equipment

Choice of equipment plays an important role in any computer vision problem. There are different kinds of cameras available in market, ranging from portable point and shoot cameras to DSLR to high cost purpose built imaging systems. However in the recent years, due to decrease in cost of technology, high quality cameras are within reach of larger subset of researchers and professionals. Initially a purpose built 3D camera by Fujifilm (FUJIFILM Corporation, 2014) was used to achieve the objectives, however, with the passage of time it was observed that this camera is not suitable for 3D reconstruction despite the purpose built nature. The reason for incompatibility is very small lens construction which makes it impossible to be perfectly smooth causing imperfections. Fujifilm 3D camera is built in a manner that it was impossible to take images independently from the right camera thus making it difficult to calibrate right camera independently. The fixed base line and rigidly fixed lens also make it impossible to change orientation and take images in the order and direction required by the user. Therefore the purpose built point and shoot cameras are not recommended for such a 3D reconstruction practice.

Figure 2.4 Fujifilm W1 3D Camera Front and Rear View (Goldstein, 2009)

2.6.1. Non Zoom vs. Zoom Lens

Cameras tend to zoom by increasing their focal length in order to make a farther object appear closer. This change in focal length affects the camera calibration; therefore, it is generally suggested to use a non-zoom lens for the purpose. In case of non-availability of non-zoom lens, the zoom of camera should be fixed and shouldn't be changed. The focus should also be fixed at infinity if possible and shouldn't be altered throughout the course of experiment.

2.7. Image processing

The purpose of image processing is to tweak images in order to obtain information from them. Image processing involves various operations that may be in the spatial domain or the frequency domain. Various elements of image processing include;

2.7.1. Raster Image;

A raster image is where images are stored in matrix form. The pixels of image are arranged in the form of rows and columns. The image is stored as a matrix of dimension M x N, where each matrix value is given by Equation 2.11.

$$I_{(x,y)} = f(x, y) \tag{2.11}$$

Where '***I***' is the Image Matrix and *x*, *y* is the position on image considering origin on the top left corner.

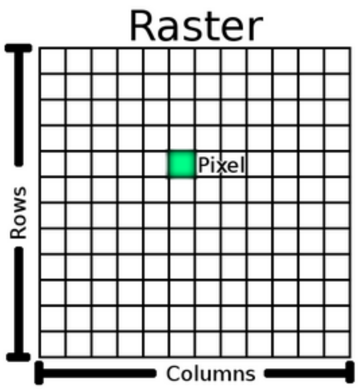

Figure 2.5 Raster Image Visual Representation (Gonzales & Woods, 2008).

2.7.2. Filtering

Filtering is the process of enhancing images in order to obtain and enhance certain details like edges etc. Various types of filters exist for the specific operations like edge detection or smoothing or data extraction etc.

2.7.2.1. Averaging Filter

Averaging operation is performed to remove unwanted noise from the image that affects further operations and quality of image. The averaging filter can be either weighted or non-weighted filter depending upon the operation. The Gaussian filter can also be used for averaging operations. The averaging filters are also known as low pass filters since they filter only the low frequencies and allow high frequencies through.

$$\frac{1}{9}\times\begin{bmatrix}1&1&1\\1&1&1\\1&1&1\end{bmatrix}\qquad \frac{1}{16}\times\begin{bmatrix}1&2&1\\2&4&2\\1&2&1\end{bmatrix}\qquad g(x,y)=\frac{\sum_{s=-a}^{a}\sum_{t=-b}^{b} w(s,t)f(x+s,y+t)}{\sum_{s=-a}^{a}\sum_{t=-b}^{b} w(s,t)}$$

Figure 2.6 Averaging Filter Mask and Mathematical Form (Gonzales, 2000)

The averaging filter applied to image removes unwanted low frequency variation in the image.

Figure 2.7 shows implementation of averaging filter on a selected row of image matrix. As it can be seen, the noise causing variation all along the length of line has decreased considerably, however high frequency changes have remained unaffected.

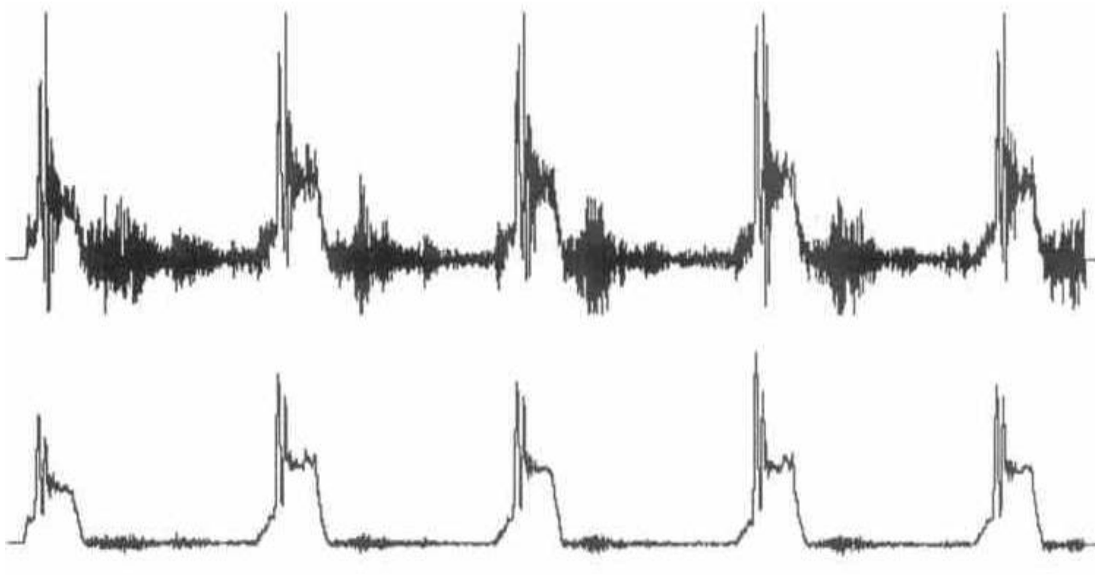

Figure 2.7 Signal before and after application of smoothing operation. (Gonzales, 2000)

2.7.2.2. Edge Detection Filter

Edge detection is used for detection of edges and corners in an image. The sobel filter is also known as gradient filter and is given by the followings relation and mask.

$$\nabla f = \begin{bmatrix} G_x \\ G_y \end{bmatrix} = \begin{bmatrix} \frac{\partial f}{\partial x} \\ \frac{\partial f}{\partial y} \end{bmatrix}$$

−1	0	1
−2	0	2
−1	0	1

Figure 2.8 Sobel Filter Mathematical Relation and Mask

2.7.3. Hough Transform,

Hough transform (Hart & Dunda, 1972) is a feature extraction technique aimed at extracting objects of a certain shape from the image. Hough transform uses a binary edge detected image as its input and creates an accumulator array of possible m and b values for each detected value of edge following the simple relation shown in Equation 2.12

$$y = mx + b \tag{2.12}$$

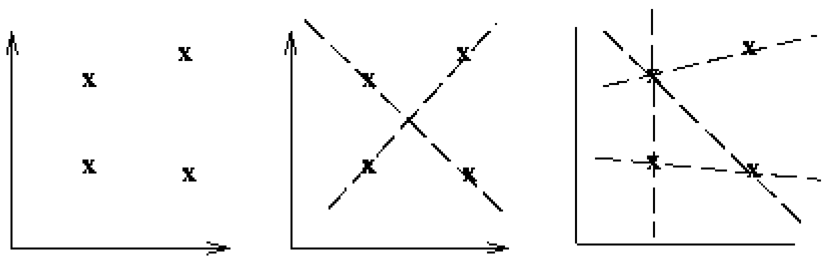

.

Figure 2.9 Hough Transform (Fisher, Perkins, Walker, & Wolfart, 2003).

The peaks in the array also known as Hough peaks provide possible orientation and shape of line object. In case detection of different shapes is desired in an image, the relation for Hough transform can be modified in accordance with the requirement. Since the lines in our problem are either vertical or horizontal, there is a chance of infinite slope which cannot be reflected in Cartesian Coordinates; therefore, it becomes necessary to use polar coordinates, which require the accumulator array to be calculated in the form of ρ and θ values which are given by the relation in Equation 2.13

$$\rho = xcos\theta + ysin\theta \tag{2.13}$$

2.7.4. Color Thresholding and Segmentation;

Color has been identified as a salient feature for object detection given that color is an effective cue for differentiating one object from another(Wada, Kaneko, & Takeguchi, 2006). This technique has been used in construction progress monitoring as well.(Son & Kim, 2010). Since structural elements have specific color, the same specific information can be used for segmentation. However, pure color data based on information of RGB band is not reliable and is affected by choice of computer graphics and illumination values (Authors, Bascle, Bernier, D, & Lemaire, D, 2006),. hue, saturation, intensity model can be explained by Figure 2.10.

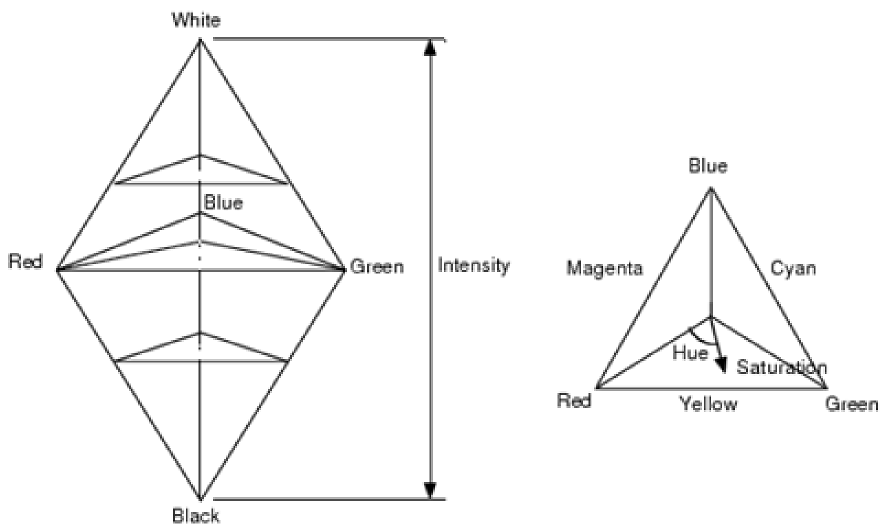

Figure 2.10 hue saturation and intensity Space (Gonzales & Woods, 2008).

In **Figure 2.10** the HSI triangle (right) is formed by taking a horizontal slice through the HSI solid (left) at any intensity. Hue is the angle measured from red, and saturation is given by distance from the axis. Hue, saturation and intensity can be attained from the model defined in **Figure 2.10** using Equation 2.14.

$$\begin{aligned} H &= \arctan\left(\frac{\sqrt{3}(G-B)}{(R-G)+(R-B)}\right) \\ Int &= \frac{(R+G+B)}{3} \\ Sat &= 1-\frac{\min(R,G,B)}{I} \end{aligned} \tag{2.14}$$

2.7.5. Thresholding and Morphological operations

Based on training data of image, the threshold values for hue and saturation were determined separately. Care should be taken to choose values that include maximum number of object pixels while including minimum number of background or foreground pixels. The hue threshold values for experiment were .06<H<.09 and for saturation threshold values were .26<.S<.39. The pixels are then displayed as a binary image containing pixel of rebars only. Some morphological operations like closing and hole filling are applied to remove discontinuities.

It is observed that saturation is more stable for differentiating the bars on basis of HSI index and, therefore, saturation values are used. Although observations of some authors (Lefèvre, Mercier, Tiberghien, & Vincent, 2002) are different in this regard and instead of saturation, hue is considered a more reliable perimeter for outdoor application. Since our experiments are carried out indoors, the difference might have been observed due to this reason.

2.8. Computer Vision

Computer vision is a subfield of artificial intelligence and has found its application in medical science, defense, GIS, industry, transportation and governance etc. It involves obtaining images and extracting information from images using computer vision algorithms.

2.8.1. Measurement of Depth Information

For measurement of depth information different techniques are available. The depth is calculated usually with images taken from more than one location followed by subsequent triangulation. In order to have correct depth information, the cameras are required to be calibrated. There are linear and non-linear techniques to obtain depth information about images.

2.9. Essential Matrix

Essential matrix computation is central to the calculation of global coordinates and reflects both camera intrinsic and extrinsic matrices. Essential matrix calculation is based on epipolar geometry of the cameras and the objects, where the rays coming from object and the translation matrix lie on the same plane, is given by the relations in Equation 2.15.

$$\widetilde{P_r'}\underline{\boldsymbol{E}}\tilde{P}_l = 0 \tag{2.15}$$

Where P_r and P_l are camera matrices and E is the essential matrix with dimension 3 x 3, which incorporates the translation and rotation between the two cameras. Essential Matrix is given by relation in Equation 2.16

$$\underline{\boldsymbol{E}} = \underline{\boldsymbol{R}}[\tilde{T}]_x \tag{2.16}$$

Where $[T]_x$ is the skew symmetric form of the camera translation matrix. The essential matrix has 9 unknowns and 8 degrees of freedom. Essential Matrix is calculated by taking 8 corresponding values from both images and taking SVD decomposition. Equation 2.17 gives the relation for computation of essential matrix

$$[x_0x_1 \ + y_0y_1 + x_0y_1 + y_0x_1 + x_0 + y_0 + x_1 + y_1 + 1] * \begin{bmatrix} E_{11} \\ E_{12} \\ E_{13} \\ E_{21} \\ E_{22} \\ E_{23} \\ E_{31} \\ E_{32} \\ E_{33} \end{bmatrix} = 0 \qquad (2.17)$$

Results of the above equation by Singular Value Decomposition tend to be unreliable due to poor numerical conditioning and, therefore, preconditioning is done by normalizing all points and post conditioning by enforcing rank 2 on essential matrix. Preconditioning is undone by multiplying the estimated essential matrix with translation matrices.

2.10. Stereo Matching

Stereo matching is a correspondence problem and requires determining the pixels corresponding to the same point in the same object in the image. Stereo matching is required to determine the essential matrix using the 8-point algorithm, where 8 corresponding points between stereo images are selected for computation of essential matrix.

2.10.1. Occlusion

Occlusion is the phenomenon where an object of interest cannot be observed due to location of imaging equipment. The objects of interest get hidden and, therefore, become difficult to detect. The phenomenon becomes increasingly pronounced when imaging is being performed for thin objects and when objects of interest start occluding each other.

2.11. Measurement of 3D coordinates.

Measurement of 3D coordinates of the objects is followed by computation of fundamental matrix and stereo correspondence mentioned above. The corresponding stereo points are plugged in the following equation to determine the 3D coordinates of image. Consider camera matrix P and P' have already been computed from the fundamental matrices and corresponding pixels for objects of interest have been determined using a stereo matching algorithm, the Euclidean coordinates X are determined by the following relation

$$\widetilde{\boldsymbol{x_1}} * \left(\underline{\boldsymbol{P_1}}\, \widetilde{\boldsymbol{X}}\right) = \mathbf{0} \tag{2.18}$$

$$\widetilde{\boldsymbol{x_2}} * \left(\underline{\boldsymbol{P_2}}\, \widetilde{\boldsymbol{X}}\right) = \mathbf{0} \tag{2.19}$$

Equation 2.18 and Equation 2.19 can be written in the form

$$\underline{\boldsymbol{A}}\widetilde{\boldsymbol{X}} = \mathbf{0} \tag{2.20}$$

Solving Equation 2.20 by taking Singular Value Decomposition of A, the 3D coordinates in the form of vector X are obtained. However, since the camera matrices computed from fundamental matrix are not unique, the obtained vector X is also not unique. Therefore, projective reconstruction has to be done in order to perform metric reconstruction from affine values. This detail is more important when objective is to obtain dense 3D reconstruction.

CHAPTER 3

METHOD

3.1. Introduction

As-built information of structural members is required to determine the actual capacity of concrete member which might be different from design capacity due to various workmanship and environment related factors. The purpose of this research is to develop a method to acquire rebar diameter, spacing and count necessary to perform structural analysis of reinforced concrete members. The as-built information needs to be acquired in an accurate and dependable manner that is free of human error. A method is developed to serve the purpose of automated acquisition of structural information of reinforced concrete columns. The technique for automation is based on computer vision which contains application of photogrammetery and image processing as well. Image processing is a technique of manipulating with image raster data to obtain information like presence of rebars, diameter of rebars and their approximate count. Computer vision deals with 3D part of method where 3D location of each bar element is determined using essential matrix, camera intrinsic and extrinsic matrices.

An algorithm is developed to determine rebar diameter, longitudinal bar diameter, longitudinal bar and stirrup spacing that are necessary to calculate the structural strength of reinforced concrete columns as well as compliance of codes. Due to nature of problems and differing degree of accuracy requirement for bar diameter and bar coordinate computation, the approach involves application of various techniques explained in the chapter in detail. The summary of algorithm is provided in the beginning followed by stepwise explanation of each part.

Various intricacies related with photogrammetry, image processing and computer vision knowledge areas need to be understood before development of a comprehensive method. The geometry of camera forms the building block of 3D objects transformation to 2D image on an image plane. The camera matrix is inherent part of the 3D vision that is determined by camera calibration experiment. The fundamental matrix computation and derivation becomes building block of all 3D vision processes.

3.2. Main Steps of Rebar Detection and Measurement Method

The main assumption for method starts with calibration of camera to determine its internal parameters. This step is followed by acquisition of image making sure that there are minimum occlusions present. Afterwards bar location are determined using hue and saturation space information followed by creation of Detected Lines along the edges of rebars. After Detected Lines to detect bar edges, bar diameter is computed using pixel width information computed from checkerboard boxes. The final step involves measurement of 3D coordinates using the computed camera extrinsic matrices and fundamental matrix. Stereo algorithm is developed specifically to match stereo points considering occlusions make it impossible for regular stereo matching algorithms to work. In the end the result is displayed along with computation error.

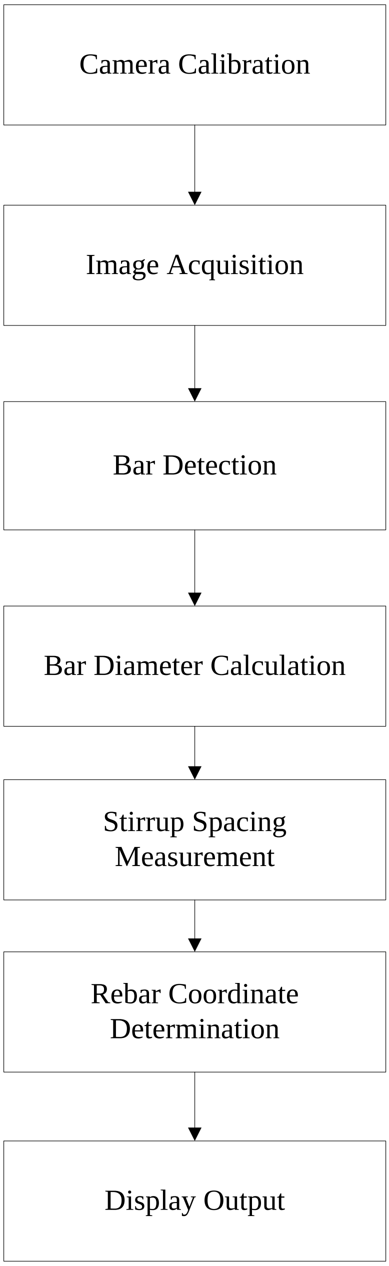

Figure 3.1 Main Steps of Bar Detection and Measurement Method

A specimen is required to test the steps of method and discuss its strengths and weaknesses in detail. Specimen is created to test the accuracy of method and measure the accuracy of automated measurements. The section of specimen is shown in **Figure 3.2**. The specimen has three rebars on each face with rectangular stirrups. Cluttering means high density of rebars that make it difficult to differentiate individual rebar element. Cluttering is avoided in order to minimize occlusions.

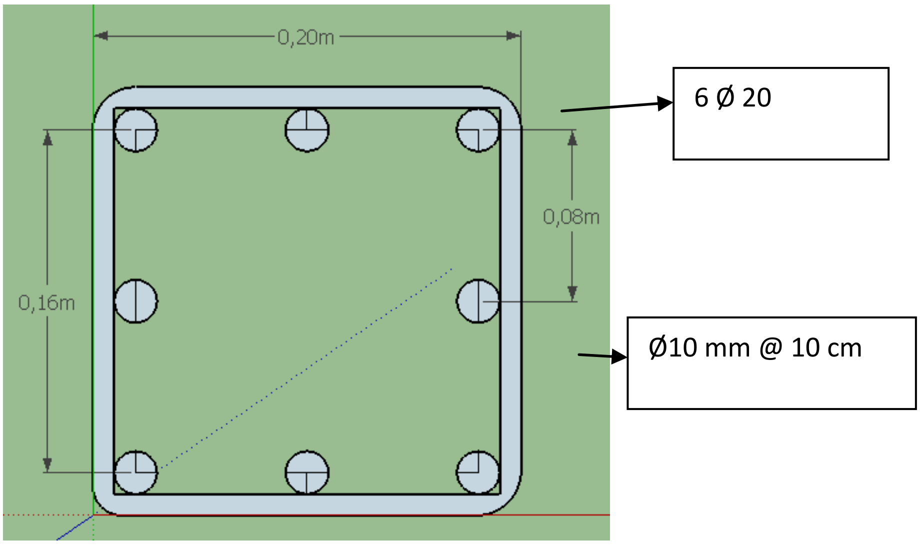

Figure 3.2 Ideal Section of Specimen for testing of Algorithm

Figure 3.3 Actual Specimen

3.3. Camera Calibration

Camera calibration was attempted with a number of calibration software (Bouguet, 12013). However considering the ease of use, cost and availability, Matlab's built-in Camera calibration functions were used for camera calibration. The camera calibration was done in following steps.

Imaging of Camera Grid.

15 images are taken of checkerboard gird from different angles and different camera orientations as seen in Figure 3.4 to create a set of images for camera calibration. The corners of a checkerboard in all images provide orientation of camera and the width of checkerboard information, that is already stored in the database, is used to determine the camera focal length, principal point as well as distortion information.

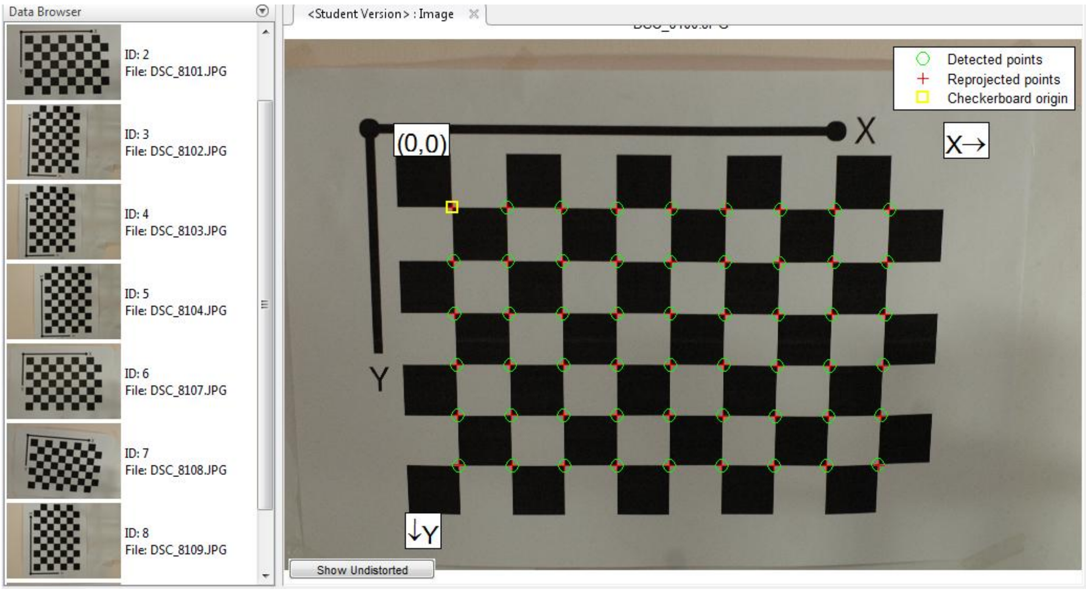

Figure 3.4 Camera Calibrator interface.

Finally the calibrator is run that calculates camera parameters according to preset information about the width of checkerboard boxes and number of boxes along x and y axis. It is important to ensure that the number of boxes along one axis is even and the other boxes are odd.

Once calibration has been done, the extrinsic plot and error histogram, shown in Figure 3.5 visualizes the quality of calibration. The error should be less than 1 pixel for best results.

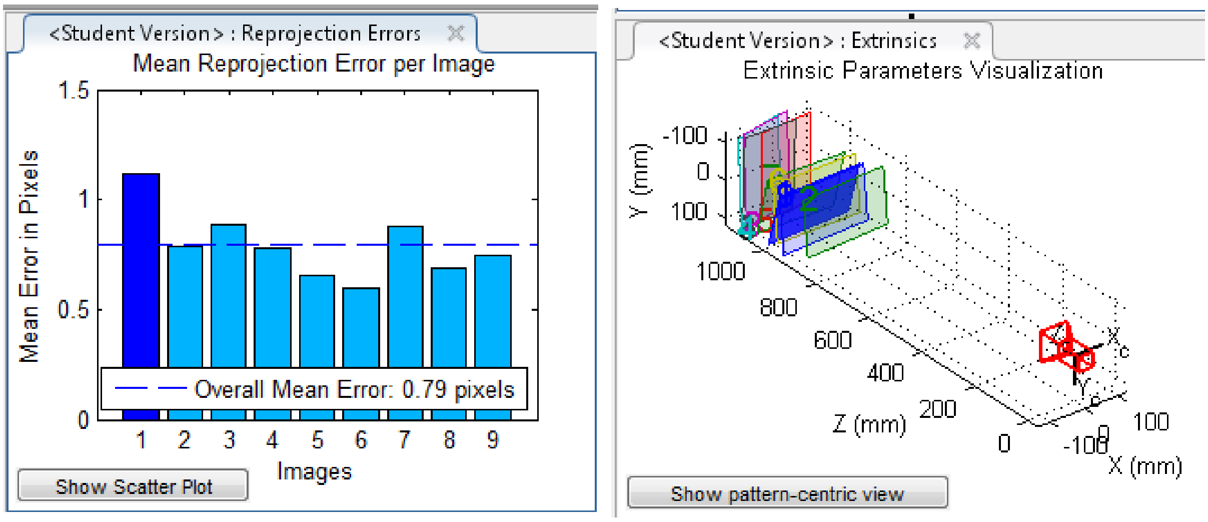

Figure 3.5 Mean square error and Extrinsic Visualization Screenshot

The image with highest mean square projection error can be checked and evaluated for error. The results can be exported in the form of camera parameters that contains camera intrinsic matrix. The calculated camera extrinsic matrix for the NIKON D70 camera with Nikor 50mm 1:1.8D lens is given by the relation in Equation 3.1.

Focal Length in term of x and y pixel height

Principal Point Coordinates

$$\begin{vmatrix} 6486.9 & 0 & 1575.4 \\ 0 & 6490 & 939.7 \\ 0 & 0 & 1 \end{vmatrix} \tag{3.1}$$

The intrinsic matrix contains the focal length and principal point components mentioned in terms of pixels. It is pertinent to note that the principal point is not located at (1500, 1000) which is the center of the CCD frame rather it is offset. These parameters are important for accuracy and can only be determined using calibration. Camera Exchangeable Image File Format (EXIF) data file contains focal length information as well and can be used to assume intrinsic parameters, however, after performing calibration it has been observed that calibration information is not accurate and may cause inaccuracies in resulting calculation. Figure 3.6 shows example of EXIF data for image shown in Figure 3.3. As seen in Figure 3.6, the focal length information is provided as well as F-Stop and exposure time information. The focal length is taken from EXIF data and principal point is assumed in the center of sensor.

Camera model:	NIKON D70	Max aperture:	1.6
Subject:	Specify the subject	Metering mode:	Spot
F-stop:	f/3.2	Flash mode:	No flash
Exposure time:	1/30 sec.	35mm focal length:	75
Exposure bias:	0 step	Date created:	19.08.2014 23:44
Focal length:	50 mm	Date modified:	19.08.2014 23:44

Figure 3.6 EXIF Data example of image of specimen

3.4. Image Acquisition

Image acquisition was performed using Nikon D70 DSLR camera with 1:1.8 50mm fixed zoom lens similar to what is shown in Figure 3.7. The focus was fixed during one complete round of imaging of the specimen starting from one end and finishing at the other end. Industry experts recommend keeping the focus fixed at infinity during imaging; however, it is not a possibility considering limited distance from the specimen.

Figure 3.7 Nikon D70 with 50mm Lens Used for Imaging (Askey, 2004)

Image acquisition is the building block of Bar Detection and Measurement Method. 2 x Stereo Images are acquired while ensuring minimum occlusions. The visibility of edges is an important aspect of the images thus there should be minimum blurring as well. The checkerboard should also be focused and be part of image. The current setup is prepared in such a manner that checkerboard is not placed far from the specimen; the top of the prepared specimen should be below the third row of checkerboard boxes. This arrangement is done in accordance with spatial search radius limitation algorithm. Any change in focus setting should be avoided during image acquisition part since any alteration would affect camera calibration thus further pronouncing errors. The F-Stop number should not be changed during the course of image acquisition thus keeping the relative aperture constant. In order to avoid very bright and very dark images, the exposure time can be varied to obtain visually images with optimum brightness.

3.5. Bar Detection

Detection of bars is done using the color thresholding information as well as the Hough transform. Figure 3.8 details algorithm for bar detection using HSI thresholding of the acquired images to obtain a binary format that contains pixels detected for rebar element. The binary image is then refined using morphological operations followed by statistical operations to determine pixels with high probability of having rebar element. The algorithm has been divided into two sub parts. The first part deals with creation of binary image while the second part deals with morphological operations and separation of rebar pixel elements from false pixel elements that are detected as rebar pixel due to their similarity with rebar pixels.

Bars being thin elements cause occlusions and tend to overshadow each other; therefore, their detection is a tricky operation that is performed by two kinds of operations. Bar detection is done either using the color thresholding information based on HSI data or the Hough transform.

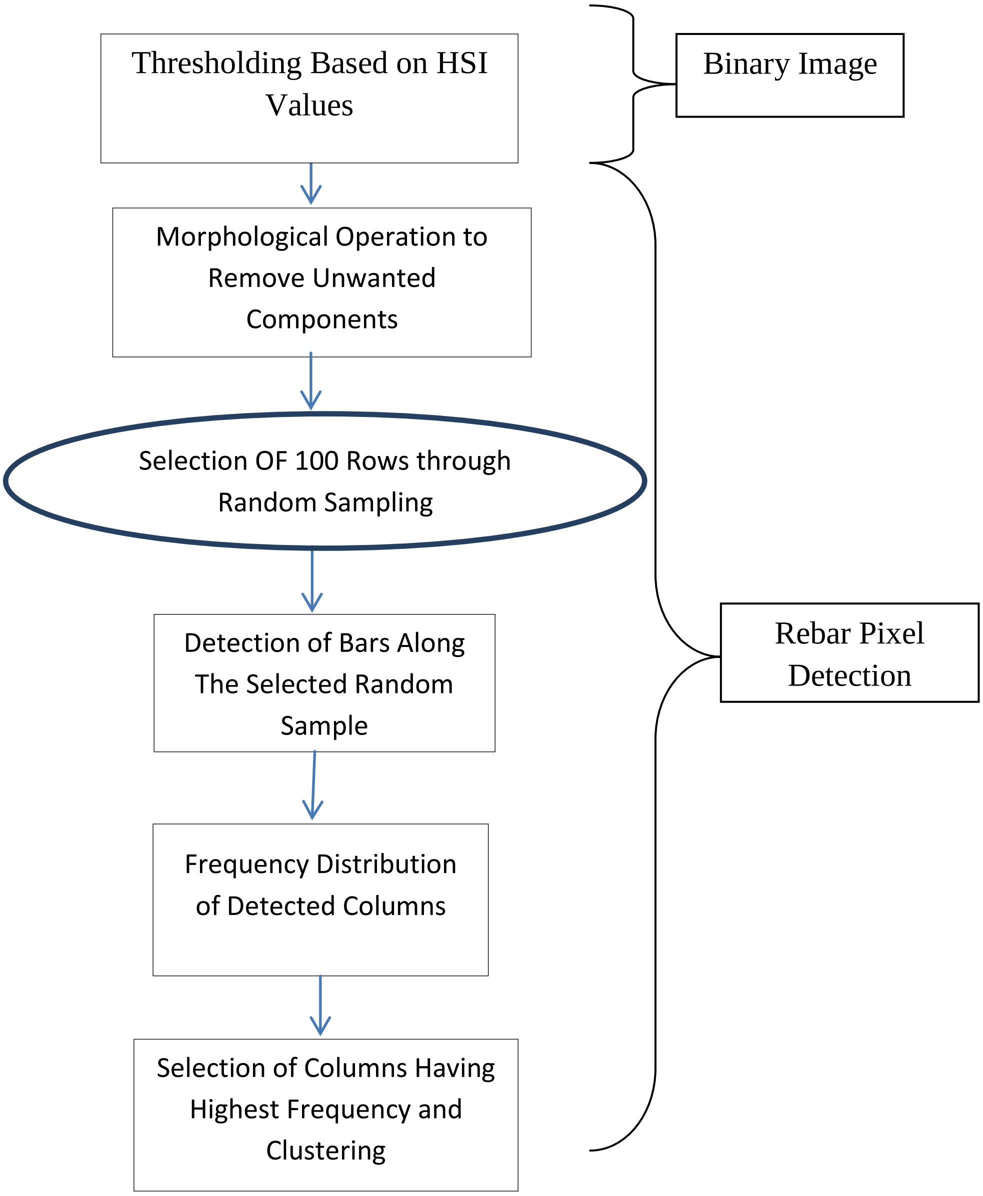

Figure 3.8 Algorithm for Bar Detection

3.5.1. Binary Image

Bar detection is based on hue and saturation values obtained from 10 training images in order to determine the range of Hue, Saturation and Intensity range of rebar pixels. Thresholding should be done in a manner that minimum pixels belonging to rebar are rejected and minimum pixels that don’t belong to rebar are accepted.

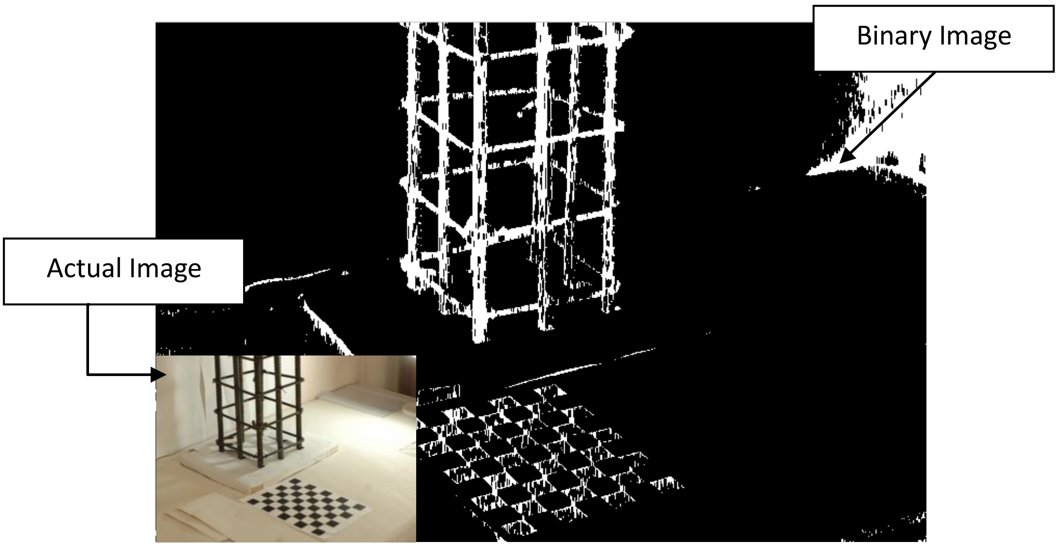

Figure 3.9 Image Thresholding using hue

The thresholding values and procedure include checking each pixel for hue and Saturation values. The pixel whose hue and saturation values fall within the range are given a value of 1 and all other pixels are given a value of zero. Figure 3.9 shows representation of a binary image of the sample specimen formed in accordance with threshold values.

3.5.2. Rebar Pixel Detection

Rebar detection is performed to count the number of longitudinal bars present in the image according to their locations. The purpose is just to provide the number of rebars and not the measurement information. The pixel in the binary image is representation of rebars in the image. Due to presence of elements with similar hue or saturation values, false pixels can also be considered as part of rebar but they are continuous along the length of rebar. Therefore a search algorithm that detects the rebars one-by-one is developed.

The search algorithm runs along the rows of image to determine the columns where bar elements are present. Then another 100 rows are randomly selected from the image and pixels with value '1' are detected in each row separately. The 100 randomly selected rows are selected below the second last row of checkerboard. A frequency distribution depicting the number of times a column is detected for each row is stored. The columns whose frequency is greater than a manually decided threshold is deemed to contain rebar pixels. The columns having frequency less than the subject threshold is rejected as background pixels are falsely detected as rebar pixels.

As a final step, clustering is performed to combine adjacent pixels representing a single rebar. Figure 3.10 shows detected bars using the presented search algorithm.

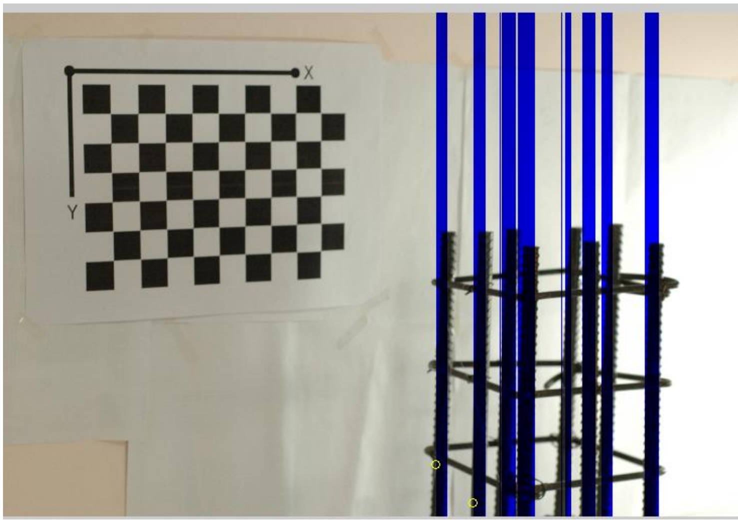

Figure 3.10 Detected Rebars using Search Algorithm.

Since the parameters used for thresholding are based on hue, saturation and intensity values; the same parameters can be used for rebar detection in various cases. This technique is more useful as compared to other edge detection based techniques for bar detection since it is not affected by background and focusing information and only uses the HSI space for pixel detection. The morphological operations are required in order to cater for pixels that belong to the rebar but are rejected. Such pixels create holes in the binary image. In order to cater for the hole, morphological operation of dilation followed by erosion is applied along with clean operation and close operation. All these operations have parameters like mask size and shape of the mask. These parameters are manually fixed and might require change in specimen or the condition.

3.6. Bar Diameter Calculation

First, width ratio of one pixel is determined using the checkerboard boxes, width of which is already known. This process is followed by determining Detected Lines which are present on both sides of rebars. Then the diameter of each rebar is calculated by measuring the number of pixels between the Detected Lines at bar edges and multiplying with Pixel Width Ratio 'W' to obtain diameter in mm. The flowchart for rebar diameter measurement is presented in Figure 3.11. Distance measured between Detected Lines will give the bar diameter as shown in flowchart shown in Figure 3.11.

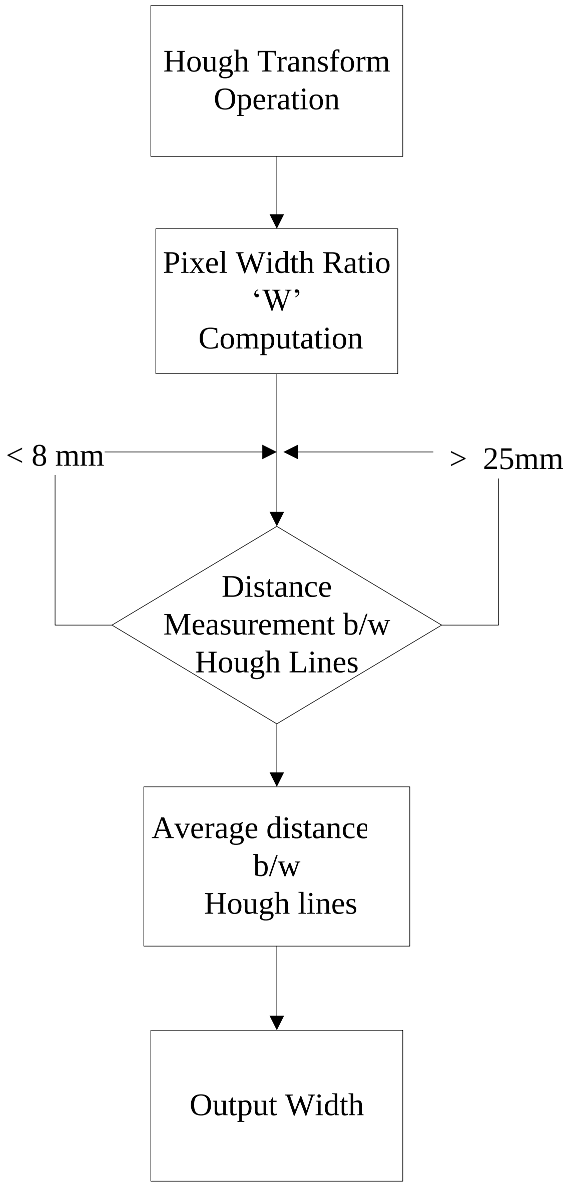

Figure 3.11 Algorithm for Bar Diameter Measurement

The detail of flowchart in Figure 3.11 is explained in following subsections. In order to reduce the computation time and false positives, the spatial search radius is also restricted. The images are taken in a manner that all rebars falling to the left of column element are ignored. Therefore search algorithm using Hough transform performs search only towards the right of the checkerboard. Similarly, in the vertical direction, the Hough transform is performed only below second row of the checkerboard. As seen in Figure 3.13, the vertical and horizontal line detection is done for longitudinal rebars only and, as seen in the subject figure, the vertical lines for checkerboard are not detected.

3.6.1. Hough Transformation

Hough transformation is applied to plot bar edges on image using edge detected binary image. The steps for Hough transformation are explained as under,

Edge detection is performed in order to determine the edges of bar elements. Sobel filter provides better results using gradient information to determine edges. Images are blurred prior to edge detection operation in order to remove noise and false information. Averaging filter is applied to remove noise and additional edges caused by presence of deformities on the rebar.

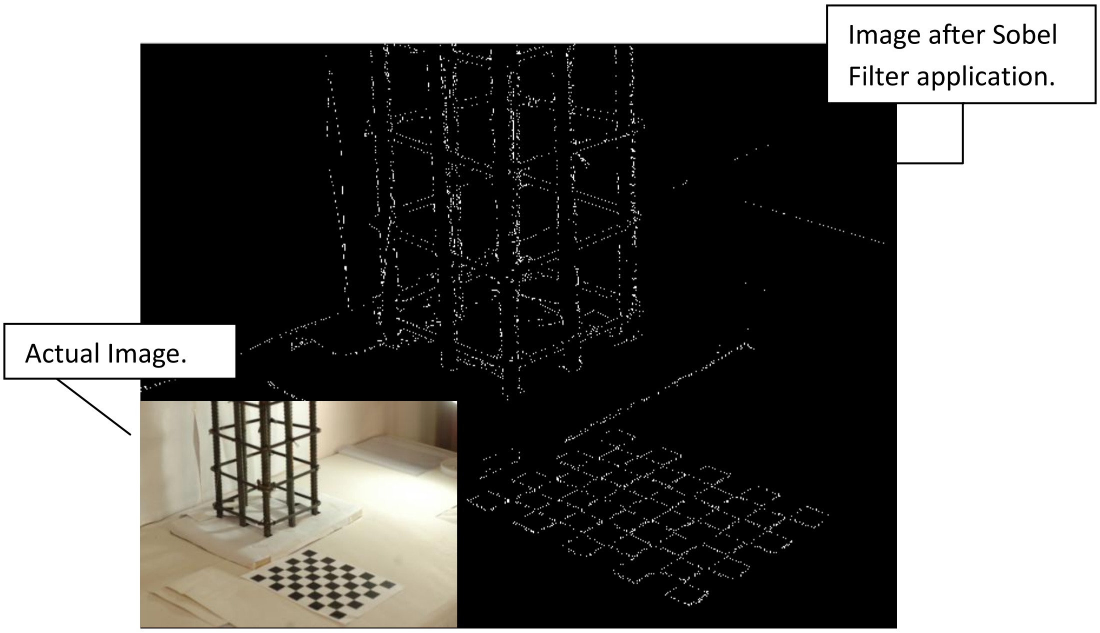

Figure 3.12 Image and its edges detected binary format with inset of actual image.

The edge detection using sobel filter is applied in both horizontal and vertical directions in order to determine the vertical rebars and horizontal stirrups. Figure 3.12 shows edge detection operation performed on the rebar image shown in the inset.

Horizontal and vertical bar edges are identified using Hough transform line detection method. Hough transform lines follow the equation of line and are governed by slope and intercept information. In order to reduce computation and false positives, the vertical and horizontal bars are detected separately by limiting the value of θ for slope computation close to $\pm 90°$ for detection of perfectly horizontal bars, and value of θ is close to 0 for detection of vertical stirrups and bars. Since our rebars in image are neither perfectly horizontal nor perfectly vertical, therefore, we use afore mentioned range of θ for both horizontal and vertical bars. Similarly the right most pixel in the checkerboard will serve as minimum value of intercept in-order to ensure that checkerboard boxes are not detected and computation time is considerably reduced. Figure 3.13 shows line detection using hough transform.

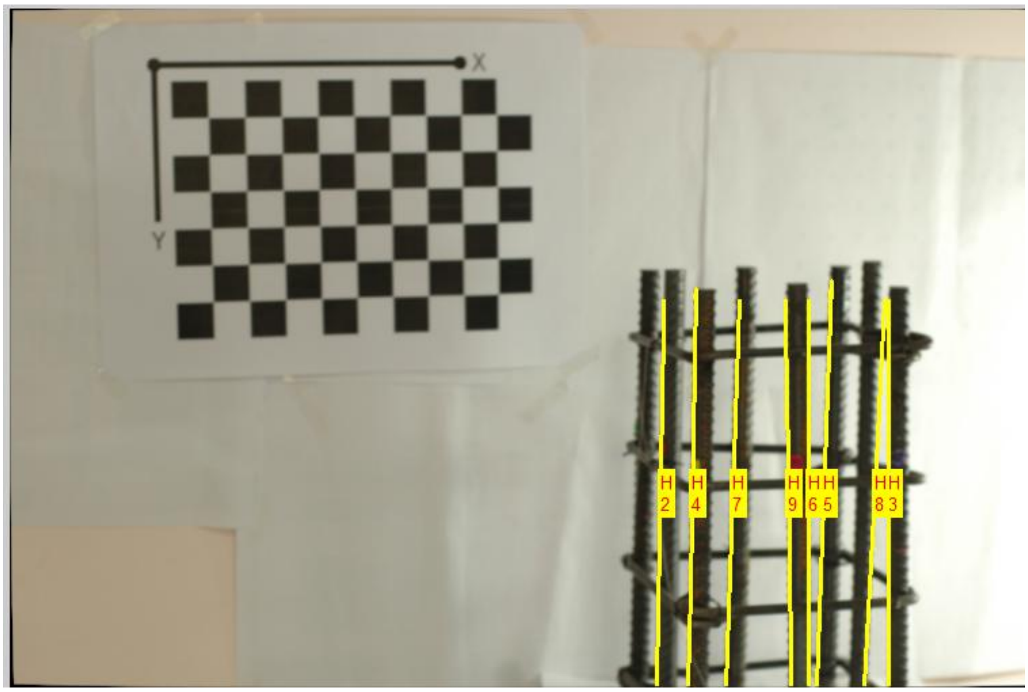

Figure 3.13 Bar detection using Hough Transform

There is a requirement to adjust the value of θ according to the angle at which the image is acquired according to the verticality of the rebars. Bar detection using Hough transform while limiting the value of θ of detected line slope in the range of

$-5 < \theta < 5$. Similarly in the next step only the horizontal bars are detected and plotted over the previous plot of vertical bars. The range of θ for detection of horizontal bars is greater since the angle of horizontal stirrups in the image is far from horizontal. The range of values is given by $\theta < -20° \ OR \ \theta > 45°$. Since the angle of horizontal bars is not constant, therefore, the range of θ is greater for horizontal rebars as compared to vertical rebars. The Detected Lines information is stored in an object oriented structure containing information about their start points, end points, slope and intercept information for further use.

3.6.2. Pixel Width Ratio *'W'* Computation

Width of pixel serves as basis of bar width measurement since all 2D measurement is based on number of pixels counted through Hough transformation technique explained above. The reference width ratio 'W' is based on width of checkerboard boxes measured in mm. Number of pixels along the width of each checkerboard box is measured. The reference width ratio of each pixel *'W'* in mm is given by

$$W = \frac{Width\ of\ Checkerboard\ Box\ in\ mm}{Width\ of\ Checkerboard\ Box\ in\ Pixels}$$

3.6.3. Bar Diameter Measurement

Width of bar requires special consideration since bar accuracy requirement is up to 1 mm and, if error is greater than 1mm, the results will provide wrong output. The bar width information is determined using the Detected Lines. The algorithm for Hough transform detects the bar edges, however, as shown in Figure 3.14 both edges of all rebars are not detected for all rebars. Distance in pixels is measured between all rebar lines and stored in an array. Those Detected Lines whose distance is greater than 25mm or less than 12 mm are rejected from computation since it is unrealistic to have rebar outside this range. Afterwards average distance measured between Detected Lines that fit decision criteria gives the diameter of rebars in mm. The computed diameter is stored in image array.

Figure 3.14 Detected Lines for diameter measurement.

In order to measure rebar diameter from detected lines as shown in Figure 3.14, the distance in pixels would be measured between H2 and H10. The pixels between rest of the detected lines are not measured since their distance is greater than the upper threshold of 25mm. The number of pixels is then multiplied with pixel width ratio already computed from checkerboard to determine the rebar diameter.

3.7. Stirrup Spacing Measurement

Stirrup spacing measurement follows the same principle as bar diameter measurement. The horizontal detected line detects horizontal stirrups and plots the line on image plane as shown in Figure 3.15. The spacing between stirrups is based on distance of horizontal Detected Lines in pixels converted to mm. The average width of pixel is already determined in mm for rebar diameter measurement. This step is followed by measurement of number of pixels between 2 horizontal Detected Lines. The minimum distance for stirrup spacing is assumed to be 5cm and any two Detected Lines which don’t fit in this criterion are rejected to avoid unnecessary computation. The average distance between Detected Lines whose distance is greater than criteria set forth gives the width of stirrups in mm.

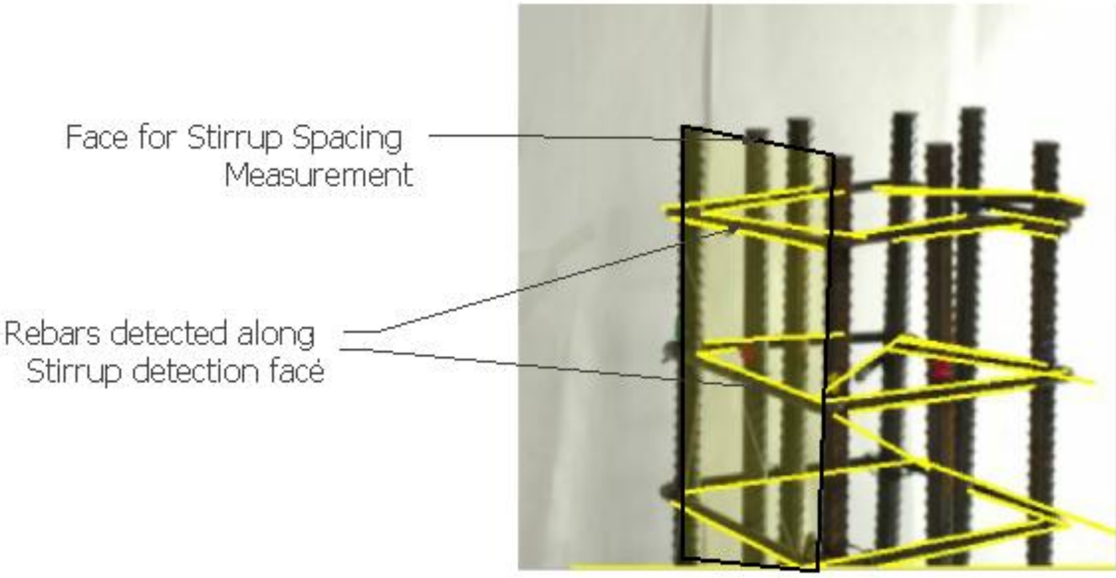

Figure 3.15 Stirrup Spacing Measurement.

Figure 3.15 shows stirrup spacing measurement using Detected Lines, As seen in figure the stirrup spacing is measured on one face only in order to attain uniform values and avoid interference from detected lines of other faces. The stirrup spacing is measured for each stirrup separately since stirrup spacing can differ from one section to other.

For measurement of stirrup diameter the same steps will be followed as those in longitudinal rebar diameter measurement. Number of pixels would be measured between Detected Lines on two edges stirrup. The number of computed pixels would be multiplied with Pixel width ratio to obtain stirrup diameter.

3.8. Computation of Longitudinal Bar Coordinates

Computation of 3D Coordinates is achieved following algorithm mentioned in Figure 3.8. The Algorithm involves calibration of camera, computation of essential matrices, and computation of camera extrinsic matrices based on imaging of checkerboard boxes. The algorithm relies on application of novel stereo matching algorithm since traditional stereo matching techniques don’t work with objects having occlusions.

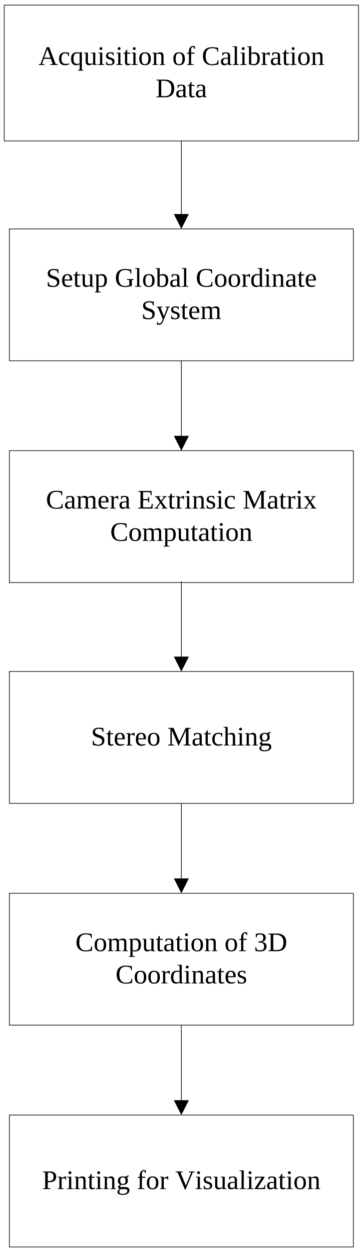

Figure 3.16 Algorithm for Computation of 3D Coordinates

Figure 3.16 gives flow chart of computation of 3D coordinates of rebars using camera extrinsic and intrinsic information. Computation of extrinsic was done using Matlab extrinsic function based on imaging of checkerboard followed by computation of functional matrix from the camera matrices. The algorithm was executed on test specimen and results are displayed.

Global coordinate axis forms the basis of measurement of rebar coordinates and is identified by the checkerboard pattern installed on the camera, which is visible in the frame.

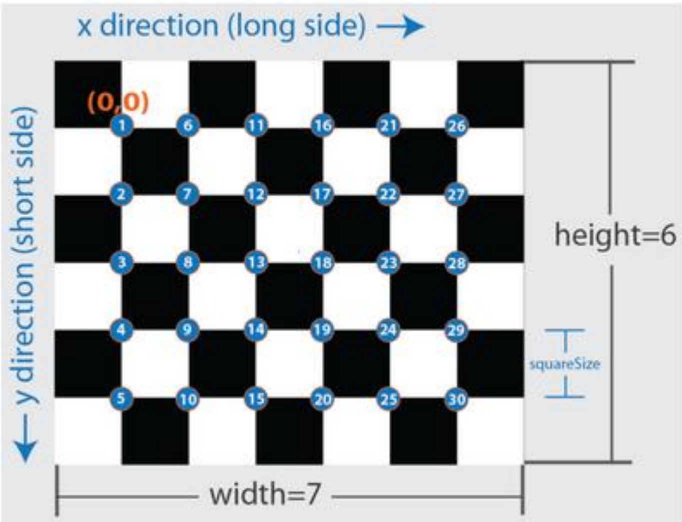

Figure 3.17 Checkerboard Pattern coordinate origin and reference

The global coordinates system with reference to the checkerboard pattern is shown in Figure 3.17. The origin marked on Figure 3.17 serves as the point of reference for all coordinate axis for all pictures taken for the particular sample. The origin serves as the local origin for the picture and can also be transformed to global coordinate system in case it exists.

Camera extrinsic matrix contains orientation and rotation of camera matrix with respect to coordinate axis. Camera extrinsic matrix is calculated by determining the orientation of camera with respect to checkerboard grid based on information about checkerboard already known. The dimension of checkerboard boxes is provided as an input in mm. The calibration grid is printed on A3 paper and fixed to a hard surface in order to maintain its shape. The size of calibration box is measured to be 31 mm and added manually. Figure 3.18 shows checkerboard boxes detected in the image. The image has been expanded for the ease of visualization.

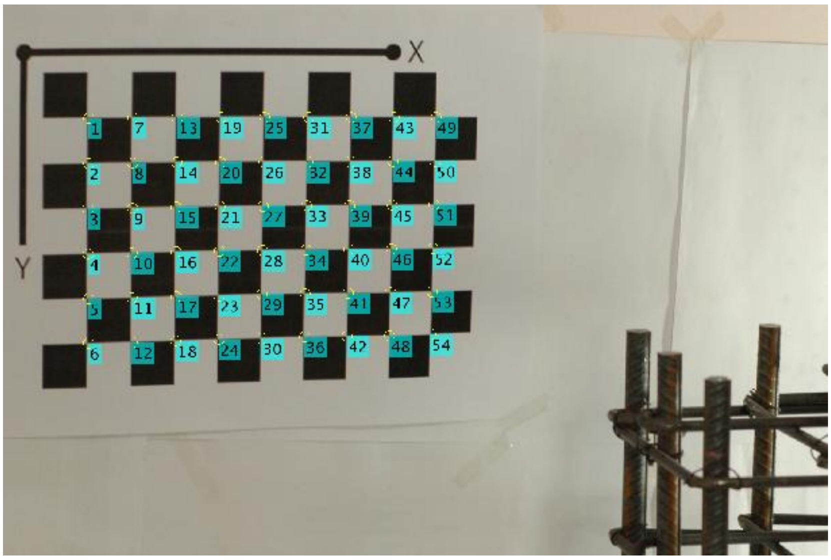

Figure 3.18 Checkerboard boxes detected and labeled

In some cases, calibration grid may not be detected because of sharp angle of image acquisition or distortion or noise present in the image. For such a case, the image has to be undistorted by using the radial and tangential distortion components obtained by calibration. Figure 3.21 shows images before and after removal of distortion. Removal of distortion is visible on the edges of image. Distortion increases with greater distance from principal point and the improvement is, therefore, visible on the edges.

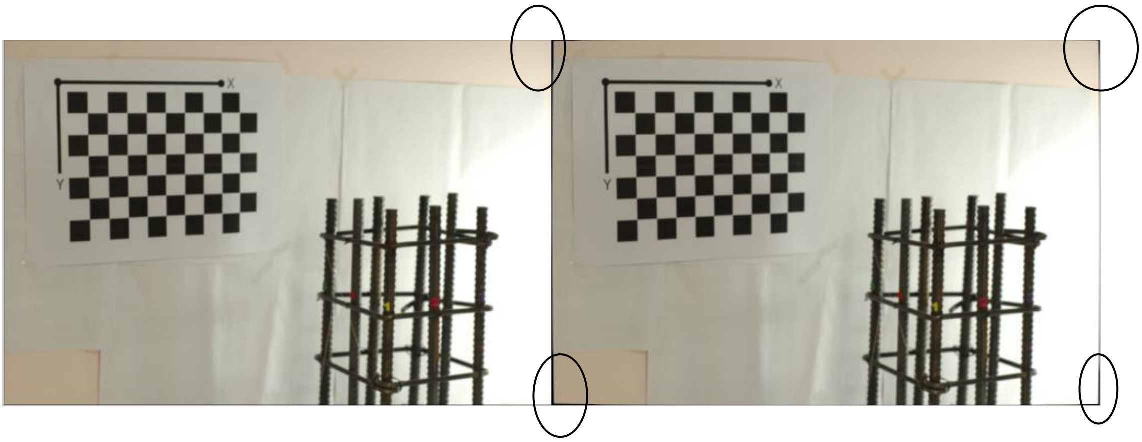

Figure 3.19 Image before (left) and after (right) removal of distortion encircled.

Once checkerboard boxes are detected and image along with world points is stored, the camera extrinsic matrix is calculated using camera intrinsic parameters obtained through camera calibration operation. The extrinsic function using the image points of calibration grid and their corresponding world points computed earlier uses it with calibration data stored as camera intrinsic parameters. The orientation of camera is attained in terms of the rotation and translation components of camera principal point with respect to checkerboard origin. The rotation and translation components of images shown in Figure 3.19 is given by rotation component 'R' and translation component 't' described in Equation 3.2 and Equation 3.3.

$$R = \begin{vmatrix} 0.9629 & -0.0226 & 0.2689 \\ -0.0319 & 0.9799 & 0.1967 \\ 0.2679 & -0.1980 & 0.9429 \end{vmatrix} \tag{3.2}$$

$$t = \begin{vmatrix} -436.4922 \\ -222.099 \\ 2298.6 \end{vmatrix} \tag{3.3}$$

3.8.1. Stereo Matching.

Stereo matching is a difficult and necessary part of the complete method. Stereo matching is required in order to find corresponding pixels in stereo images necessary to determine 3D coordinates of the objects representing the respective pixels. Stereo matching can be done automatically as well as manually using seed points. Presence of occlusions and complete symmetry make it difficult for any stereo matching algorithm to provide perfect matches. Therefore, the technique developed using functional matrix information is relied upon. Therefore, a novel technique was developed to attain stereo matching using the detected lines intersection and fundamental matrix.

Following the principal of coplanar epipolar lines and definition of fundamental matrix, if image coordinates in stereo image 1 written in homogeneous form is given by X_1 and in image coordinates in image '2' written in homogeneous form is given by X_2 and fundamental matrix is given by 'F', then according to definition of Fundamental Matrix Equation 3.4 should be adhered.

$$\widetilde{X_1}^T * \underline{\boldsymbol{F}} * \widetilde{X_2} = 0 \tag{3.4}$$

In order to compute stereo matching, Detected Lines are computed using the Hough transform. The technique involves extension of Hough transform line and subsequent calculation of intersection points of all horizontal Hough transform lines with vertical Hough transform lines followed by determination of closest point based on Equation 3.2. Figure 3.20 gives stereo matching algorithm flow chart that will be explained in this section in detail.

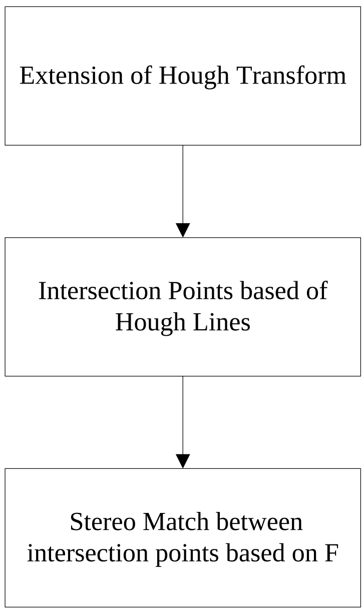

Figure 3.20 Stereo Matching Algorithm

The Hough transform lines are broken and discontinuous; therefore, they don't run along the entire length of rebars. This is caused by local noise, false edges and overlapping of bars over one another. The horizontal and vertical Detected Lines are made continuous by extending them using their slope and intercept information up to the spatial search radius limits. The slope and intercept coefficients of Detected Lines are used to extend Detected Lines to the axis of transformed coordinate system.

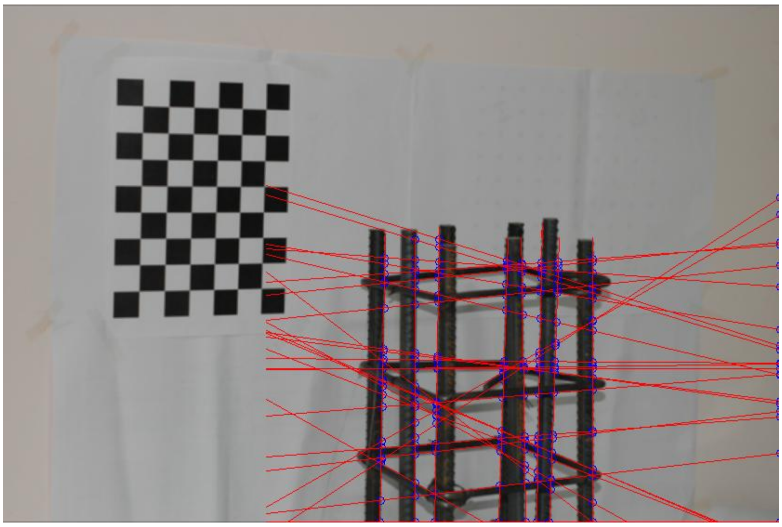

Figure 3.21 Extension of detected lines to spatial search radius.

Figure 3.21 shows extended Hough transform lines and, as seen in the subject figure, the line doesn't go beyond the first vertical row of the checkerboard boxes; this is done to avoid cluttering and unnecessary computation.

Intersection of Detected Lines is calculated based on the intersection and slope coefficients of Detected Line elements. The intersection points are determined following the principle of intersecting lines and information is stored in an array. The 'for loop' is run for every combination for vertical and horizontal Detected Lines and intersection points are plotted as shown in Figure 3.21. In order to compute nearest match, the intersection points are iteratively put in Equation 3.5 and the result is stored in an array 'Val' given by relation

$$\boldsymbol{Val} = \widetilde{\boldsymbol{X}_{\boldsymbol{1}}^{\boldsymbol{T}}} * \boldsymbol{F} * \widetilde{\boldsymbol{X}_{\boldsymbol{2}}} \tag{3.5}$$

Ideally for perfectly matching points, the result of Val should be equal to zero. Therefore, the min (Val) corresponds to the perfectly matching points. The matching points are plotted in both images as shown in Figure 3.22; the matching is very accurate and can be confirmed visually.

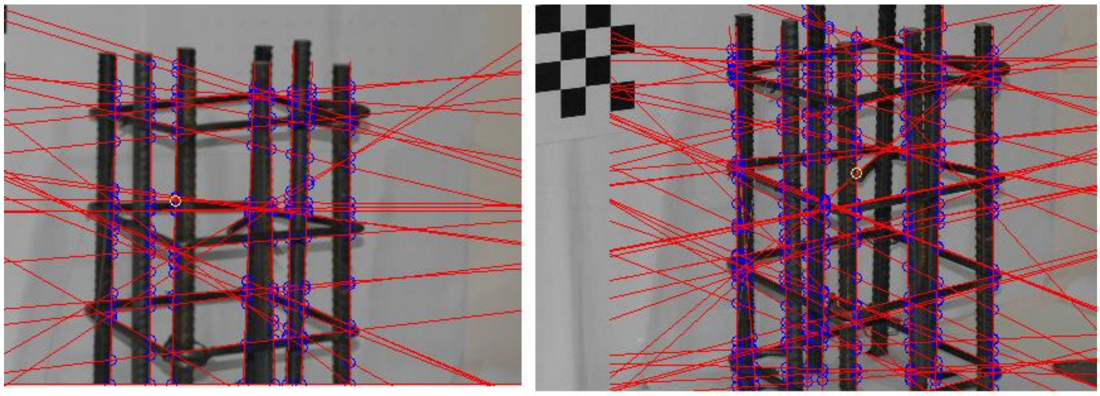

Figure 3.22 Matched Points in Stereo Images

The matching is done for each vertical and horizontal line element and results are stored for 3D reconstruction. Matched points are shown in Figure 3.23.

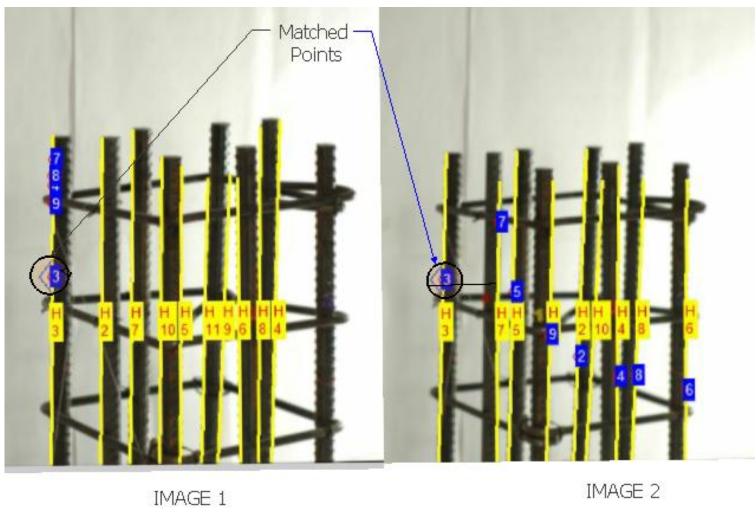

Figure 3.23 Matched Detected Lines using Intersection Points

Once the points are detected, the Detected Lines corresponding to the points represent the same rebar in both images. Figure **3.23** shows matched Detected Lines from selection of point on the basis of Equation 3.5.

3.8.2. 3D Reconstruction

The next phase is obtaining 3D coordinates of rebars using information stereo matches and camera extrinsic information obtained by using triangulation (Hartley & Zisserman, 2004). The stereo information in the form of matched point and camera matrices containing the intrinsic and extrinsic information are given as input to the triangulation part of the algorithm that determines the 3D coordinates of respective rebars one by one. The equation of camera matrices image points and camera coordinates is written in the form $x = PX$ for image 1 and $x' = P'X$ for the second image. Where x is the image coordinate of an object having 3D real world coordinates **'*X*'** in Camera having Camera Matrix given by a 3 x 3 matrix P. The global coordinate of the object will not change, however, the image coordinates of the object will change depending upon the location and orientation of the camera. For the above camera matrix, image coordinates and real word coordinates are given by Equation 3.6.

$$\boldsymbol{\tilde{x}} \times (\underline{\boldsymbol{PX}}) = \boldsymbol{0} \tag{3.6}$$

$$where \quad x = \begin{vmatrix} x \\ y \\ 1 \end{vmatrix} \quad ; \qquad P = \begin{bmatrix} P_1^T \\ P_2^T \\ P_3^T \end{bmatrix}; \qquad PX = \begin{bmatrix} P_1^T X \\ P_2^T X \\ P_3^T X \end{bmatrix}$$

Where P_i is the ith row of Camera matrix P and x,y are coordinates of the object on image plane. Substituting and combining values of camera matrix from first image and second image in Equation 3.6, we get the heterogeneous system $AX = 0$ given by Equation 3.7.

$$\begin{vmatrix} xP_3^T & -P_1^T \\ yP_3^T & -P_2^T \\ x'P_3^T & -P_1'^T \\ y'P_3^T & -P_2^T \end{vmatrix} X = 0 \tag{3.7}$$

Equation 3.7 is decomposed using Singular Value Decomposition. Picking the singular value corresponding to smallest singular value gives the coordinates *'X'* for corresponding object in global coordinate system. The matching point on both stereo images are selected manually for greater precision and since stereo matching is unable to provide matching for all rebars in both set of images.

3.9. Display Results

In the end, results are displayed in a graphical format for further use. The coordinates obtained are transformed to local coordinate system with origin location at bottom left end of the column for display purpose. The information is then displayed in a format shown in Figure 3.24.

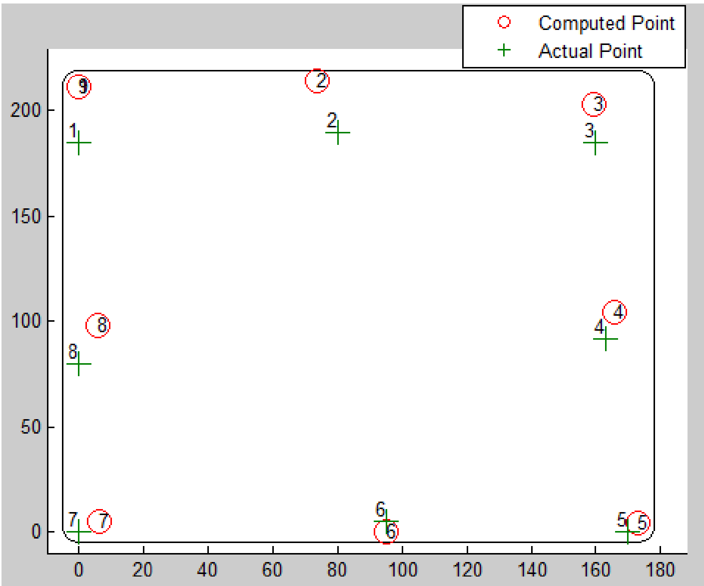

Figure 3.24 Result Output in a Graphical Form

The method developed to achieve objectives of the study consists of various algorithms each of which performs its specific function like bar detection, bar diameter measurement, stirrup spacing measurement and computation of 3D coordinates. The final result is displayed in the form of a plot for visualization.

CHAPTER 4

RESULTS & DISCUSSION

4.1. Introduction

Information regarding as-built structure is pivotal for code check, structural viability analysis, and post-earthquake or disaster structural serviceability assurance and for expansion/ demolition planning. Current method of as- built information acquisition depends on manual human input which is both time consuming and prone to human error. Image processing and computer vision are upcoming fields that have vast application in defense, robotics, medical science and management etc. A method has been developed to detect and measure Reinforced Concrete Columns information using computer vision technique. The method is divided into separate algorithms each of which performs separate tasks. The rebar detection algorithm uses HSI model to obtain rebar location based on thresholding of pixel values. The bar diameter measurement algorithm uses Hough transformation to measure rebar edges and compute number of pixels between them. The checkerboard pattern present within the image provides width ratio of one pixel. This information is used to measure rebar diameter from pixel count. The stirrup spacing is measured using the horizontal Detected Line and pixels between them, following the same 2D process for measurement. The 3D coordinates of rebars are measured using the camera calibration information containing intrinsic parameters of camera and camera extrinsic parameters obtained from checkerboard points. In order to compute 3D points in a fully automated manner, the 3D points are matched by a stereo matching technique developed specifically to deal with hollow rebar structure. The 3D coordinates are then computed by Singular Value Decomposition of Camera Matrices. The computed results are then displayed in a scatter plot showing locations of rebars.

This chapter deals with parametric study of results obtained through presented method. The algorithm is applied by varying one parameter while keeping all others constant. The effect of parameters on error of measurement is discussed for each section separately.

The developed method consists of a number of algorithms that combine to provide the desired results. The algorithm consists of image acquisition, image processing and coordinate computation parts. Each part has its own strengths and weaknesses that will be discussed in the sub sections in detail. In order to achieve maximum accuracy, special care needs to be taken during acquisition operations. Although limited, there are certain hard parameters that are required to attain best results from the specimen at hand.

4.2. Test Specimens to Test Algorithm Performance.

In order, to determine viability and robustness of the method that has been developed, the algorithms of the developed method have been tested in various steps of the algorithm. The ideal sections of Specimen # 2 and Specimen # 3 are shown in Figure 4.1 and Figure 4.2.

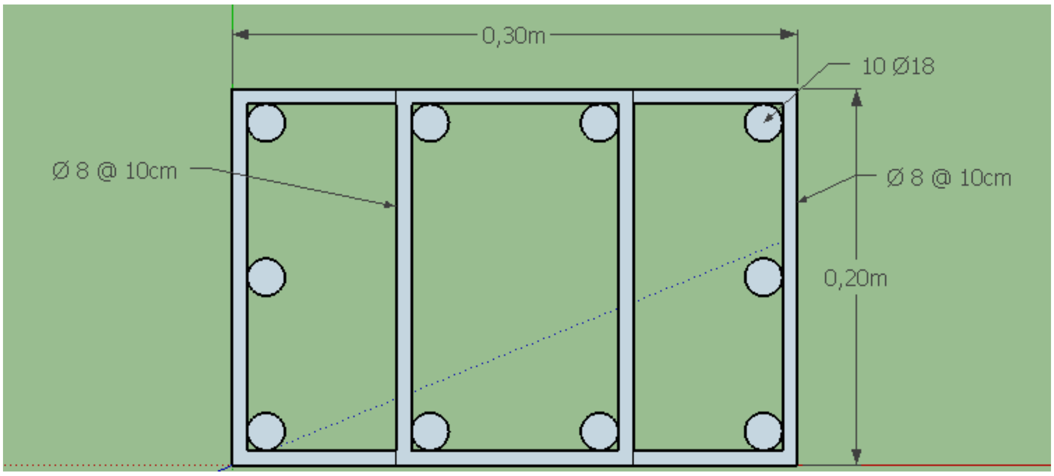

Figure 4.1 Ideal Section of Specimen # 2.

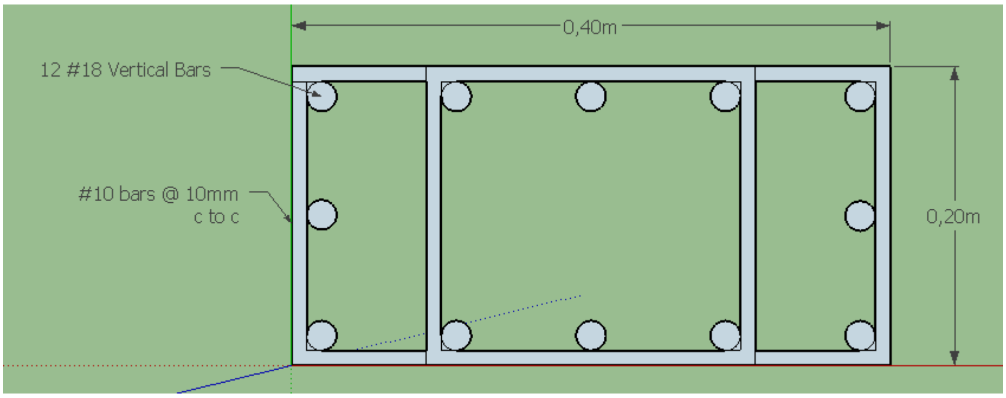

Figure 4.2 Ideal Section of Specimen # 3.

These specimens have varying width and spacing between longitudinal rebars. Each part of algorithm is separately applied to each specimen and results are evaluated and shown in upcoming sections.

4.3. Rebar Detection

Once the image has been acquired, the first operation is averaging that tends to remove false information in order to attain correct edge information. Gaussian averaging filter is used to perform averaging operation. Care should be taken that image is not over blurred otherwise real edge information is lost.

The thresholding information is based on a set of hue and saturation range obtained from a set of images. The hue and saturation space is used instead of color space because color values are affected by display adapter specifications and amount of incident light. However, the problem with using hue and saturation values is presence of elements in the image frame having similar hue and saturation values as the rebars. Although check involving both of the mentioned parameters should be able to remove maximum amount of false information, however, practically this is not the case and false information does become part of the image. Also a large number of pixels that are not part of rebar are ejected.

Rebar detection is done using hue, saturation and intensity information. Rebar detection is done to extract rebar information from image based on material identification by color thresholding. Rebar detection is applied on Specimen # 1 as well as Specimen # 2 and Specimen # 3.

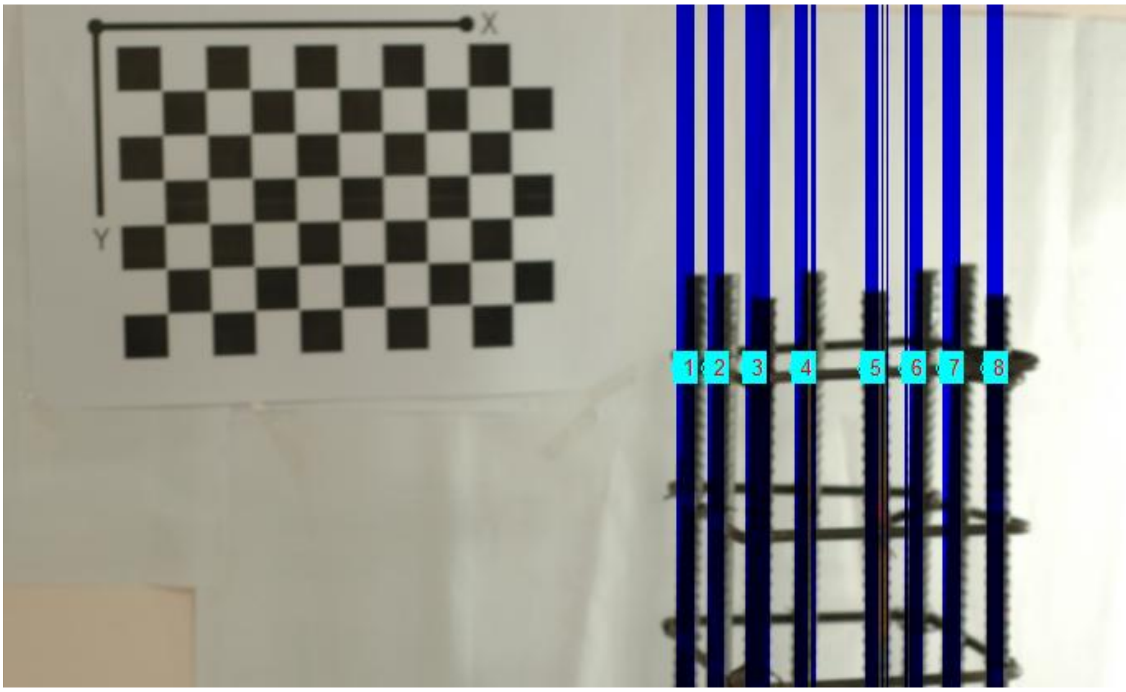

Figure 4.3 Application of Bar Detection on Specimen # 1

Figure 4.3 shows application of bar detection algorithm on Test Specimen # 1. As seen in the figure, the algorithm detects all 8 rebars present in Specimen # 1 correctly and on the right location. The correct result is due to rightly matched threshold values that were decided on the basis of training data as well as less amount of rebars density in the specimen that has caused minimum amount of occlusion in the rebar. The threshold values used for differentiating background pixels from rebar pixels are shown in Table 4.1. Since the threshold values are hard coded parameters, these values require adjustment on the basis of indoor lighting, quality of image acquisition sensor as well as amount of noise present.

Table 4.1 Hue and saturation threshold values

Color Space Property	Lower Limit	Upper Limit
HUE	.06	.09
SATURATION	.26	.39

Figure 4.4 shows application of Rebar Detection algorithm to Specimen # 2. As seen in the figure, 10 rebars are detected by the algorithm which is equal to the actual number of rebars in the specimen, but careful evaluation shows that bar 2 and 3 represent the same bar while the rebar behind bar no. 8 in Figure 4.4 is not detected and labeled.

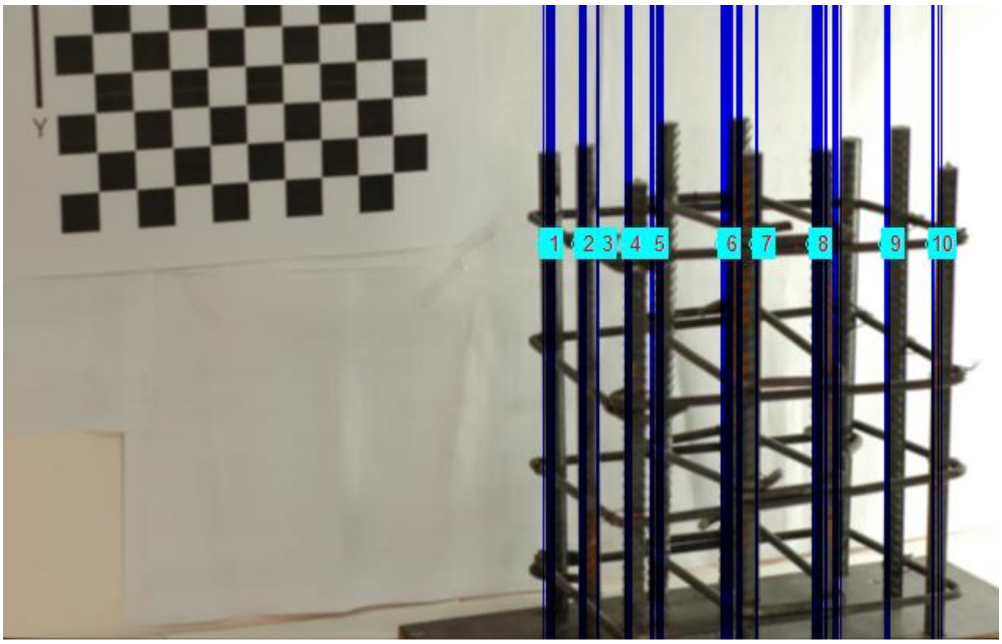

Figure 4.4 Rebar Detection in Specimen # 2.

The wrongly detected rebar is due to holes present in binary image due to rebar pixels considered as background pixels. The continuous empty space tends to create an impression of 2 rebars. The rebar next to rebar #8 is missing due to combination of poor focus of the rebar and its overlap with rebar No. 8.

Figure 4.5 shows bar detection application in Specimen # 3. As seen in Figure 4.5, the bar detection algorithm detects 12 bars in Specimen 3, which is accurately the number of bars present in the subject specimen. However, after careful observation it is seen that the bar detection algorithm has missed one bar and detected same bar as bar 9 and 10. The bar is missed because Specimen # 3 has large number of bars. Also during thresholding operations there are a number of rebar pixels that were missed causing a continuous gap between the rebar pixels making bar # 10 appear as 2 rebars.

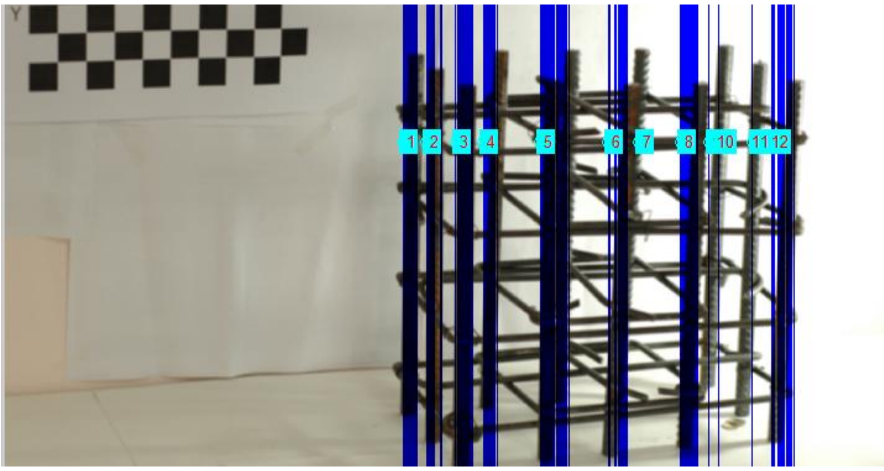

Figure 4.5 Bar Detection in Specimen # 3

It should be kept in mind that the threshold values are taken during daytimes with a combination of artificial and natural lighting. Image taken under artificial lighting will require different threshold information.

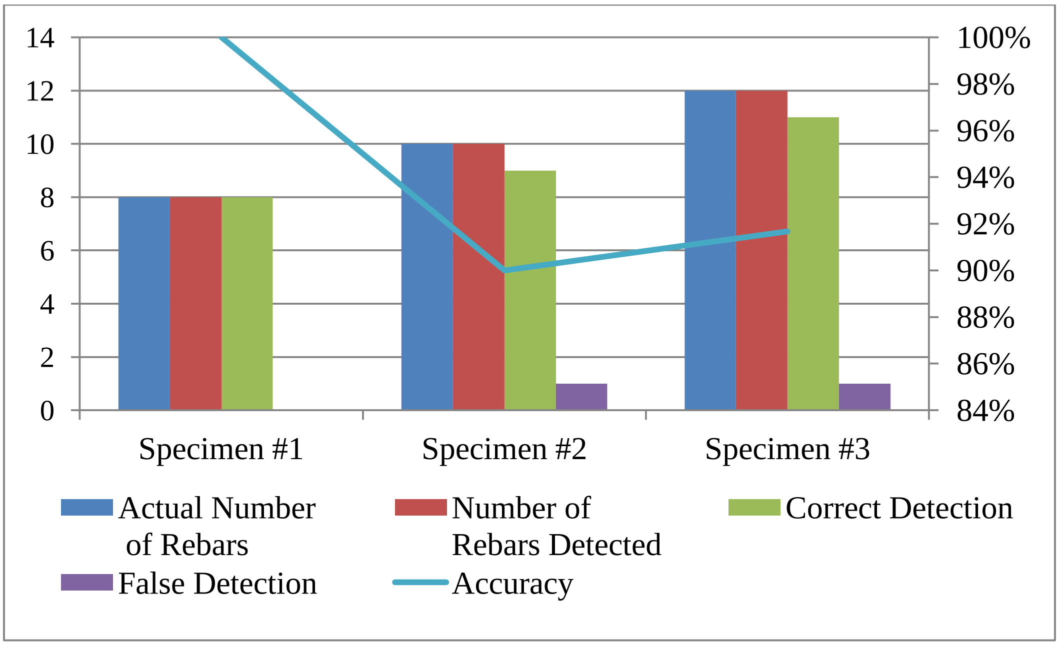

Figure 4.6 Accuracy of Rebar Detection on Test Specimens.

4.4. Rebar Diameter Measurement

Image acquisition requires special consideration and forms the basis of rebar diameter measurement. Image should be well focused, taken in good lighting conditions with sharp edges. All kinds of image sharpening and built-in camera algorithms, that automatically restores pixels, tend to create false information that is not part of original image.

Occlusions play an important role in performance of the algorithm. If the distance is increased considerably, the issue of occlusion is further pronounced. The algorithm uses 2 images for reconstruction and calculation of image coordinates, however, multiple images are acquired and the best ones with clearly focused grid and minimum occlusion are chosen for the imaging operation. Figure 4.7 shows occlusion in image caused due to overlapping of image over each other causing visibility of less number of rebars than what should actually be there.

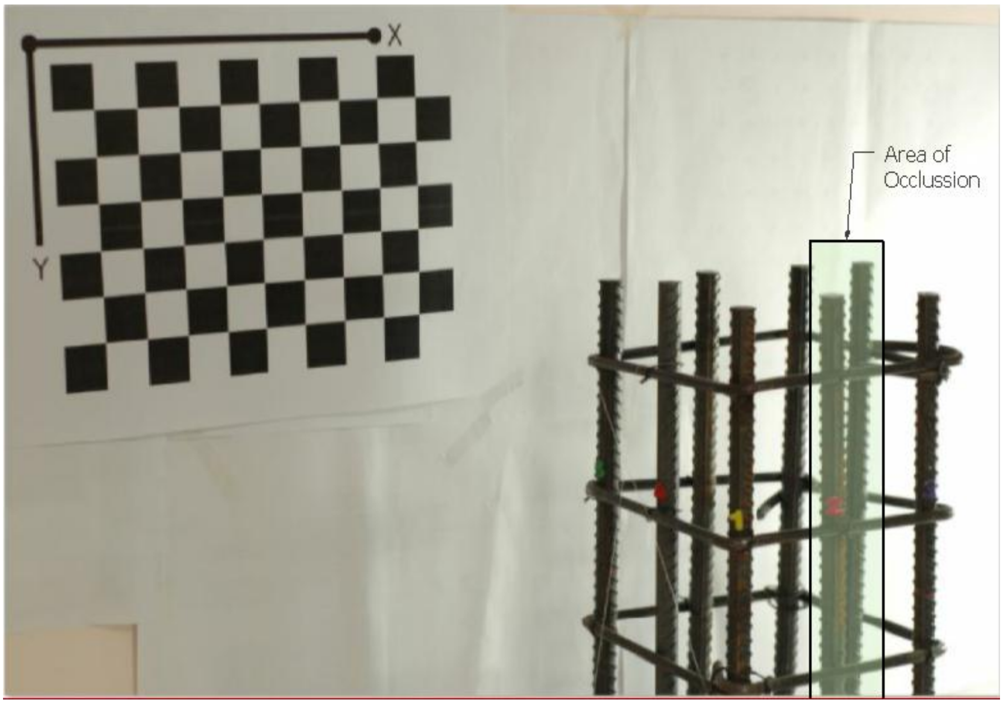

Figure 4.7 Area of Occlusion in Image

Images should be taken in a manner that all rebars are visible in the image and no rebar is hidden behind the other. The rebar should appear as straight as possible during the course of imaging and the grid should be visible in all images.

Even if there is no overlap, the occlusion creates error in rebar diameter measurement. Figure 4.8 shows representation of rebar edges detected using Hough plot. As seen in the Figure 4.8, pixels between Detected Line 10 and Detected Line 5 would give correct rebar diameter. Also pixels between Detected Line 11 and Detected Line 9 would give correct rebar diameter for image 1. while the pixel distance between rebar 5 and 6 would give incorrect diameter information for image 2.

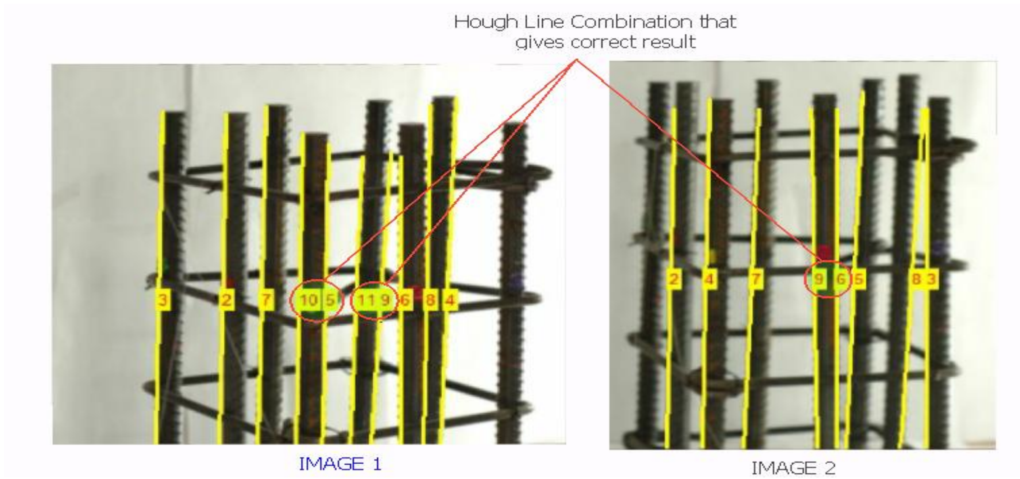

Figure 4.8 False and Correct Rebar Edges detected.

The algorithm for rebar diameter measurement detects rebars using edge information and hough transform. The rebars detected following steps of diameter measurement algorithm for images shown in Figure 4.8 are given in Table 4.2. The Lines combination underlined in Table 4.2 represents correct rebar edges while the rest of the combination represents false edges.

Table 4.2 Lines detected as Rebar Edges

Rebar Detected by Algorithm for Width Measurement	Detected Lines representing rebars in Image 1	Detected Lines representing rebars in Image 2
1	4,5	8,3
2	**10,5**	6,5
3	9,6	**9,6**
4	6,8	
5	**11,9**	
6	5,11	

As seen from the table, all rebars detected are false except the rebar 2 and rebar 5 for image 1 and rebar 3 for images 2 shown in Figure 4.8, The result of falsely detected rebars would be a wrong output of rebar diameter. It can be seen that Image 2 shown in Figure 4.8 doesn't have any rebar overlapping the other, however, occlusion due to location of posterior bars location in 2D images, the algorithm is considering empty spacing between rebars as a rebar element. Figure 4.9 shows error in image 1 and image 2 of rebar diameter calculation and it is observed that color error in computation of rebar diameter in Image 1 is less than error in computation of rebar in image 2. Although checks are applied to avoid detection of longitudinal rebars having diameter less than 15mm and greater than 25mm, yet the spacing between rebars seen in 2D image falls within the thresholds and ,therefore, their values are not ignored and are included in averaging operation done to calculate rebar diameter.

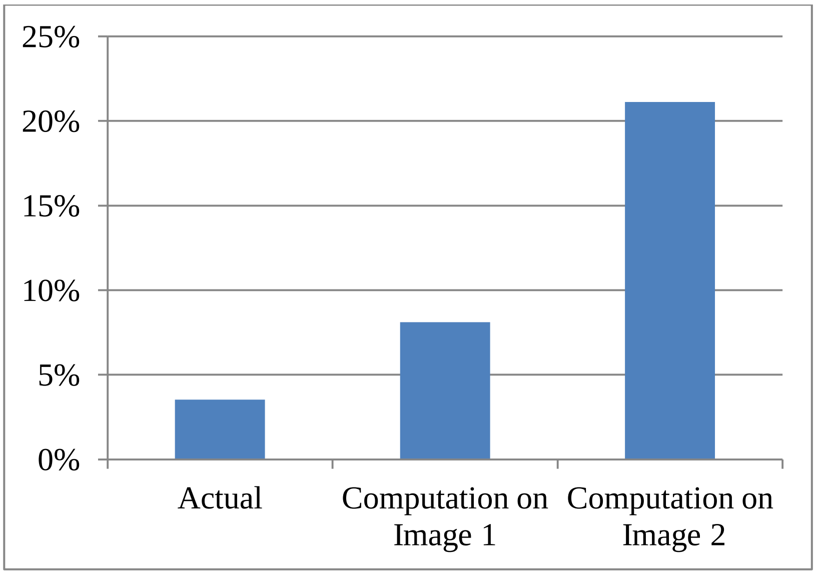

Figure 4.9 Error of Images with false Detected Lines due to occlusion

It should be kept in mind that rebar diameter is a discrete value, therefore, irrespective of the calculated diameter it needs to be rounded to the nearest commercial bar size.

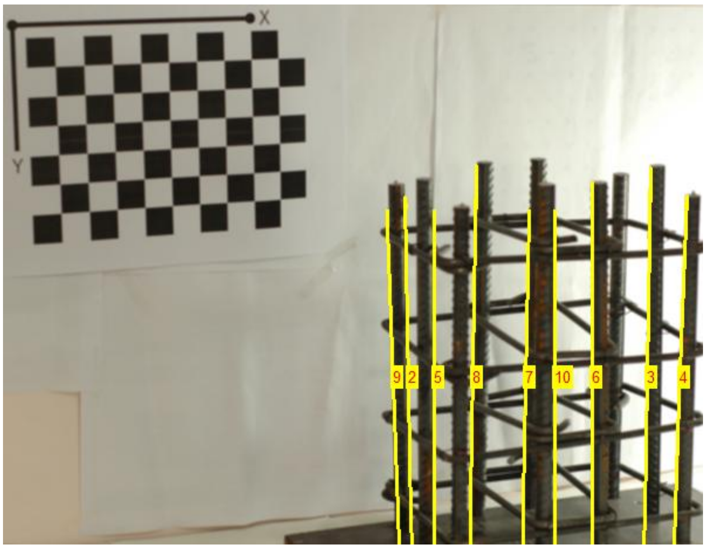

Figure 4.10 Longitudinal Bar Hough Transform for Specimen # 2.

Figure 4.10 shows lines plotted on image of Specimen # 2 for rebar diameter measurement. The algorithm has measured number of pixels between Detected Line 9 and Detected Line # 2 in Figure 4.10 to compute rebar diameter. The diameter obtained for 18mm rebar is 17.008mm. Since rebars diameters should belong to a set of discrete measurement, the rebar diameter is given nearest discrete value which is 18mm.

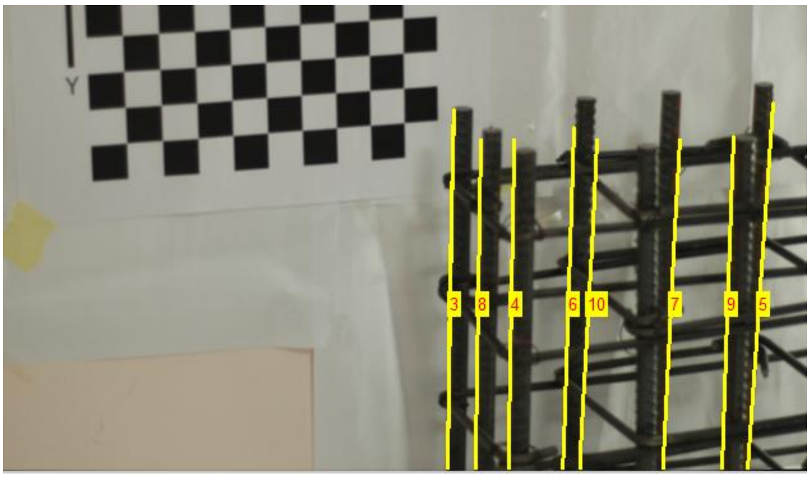

Figure 4.11 Longitudinal Bar Hough transform for Specimen # 3.

Figure 4.11 shows Hough transform application for Specimen No. 3. Image is taken closer than other specimens due to large number of rebars and inability to attain single rebar with Detected Lines on both ends. The algorithm automatically determines Detected Line 6 and Detected Line 10 as lines that are present on both ends of rebar and rejects the rest since the distance between rest of the Detected Lines is greater than commercially available rebar diameters. The pixels are counted between the rebars and the diameter obtained is 17.681mm.

The error in rebar width measurement from Specimen 1, Specimen 2 and Specimen 3 are plotted in Figure 4.12. The error is based on diameter measurement from one image.

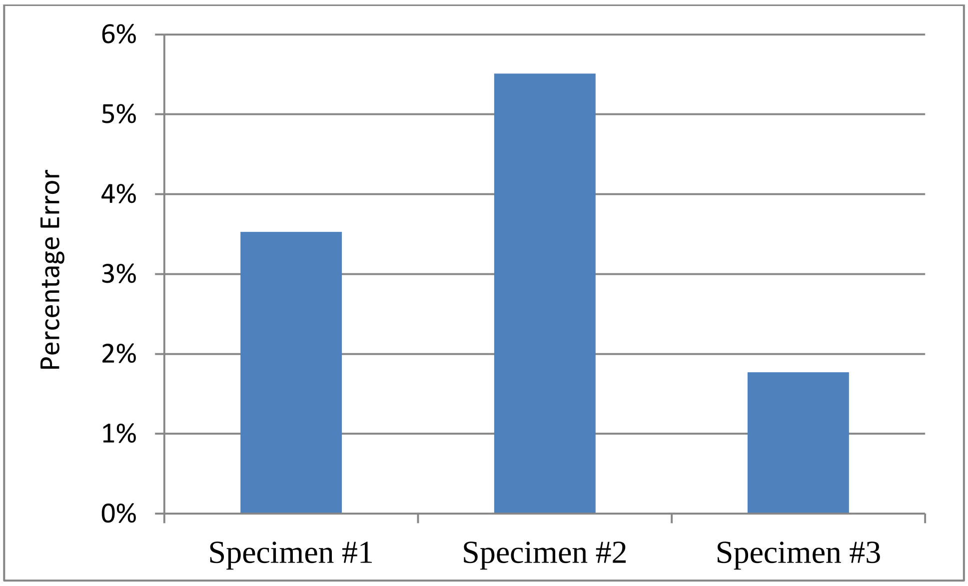

Figure 4.12 Error in Rebar Diameter Measurement

As seen in Figure 4.12, the error is not dependent on type of specimen being used; rather it is dependent upon the identification and location of Detected Lines and occlusion present. Occlusion is the most important factor in rebar diameter measurement.

4.5. Stirrup Spacing

Focusing is an important aspect of imaging. Poor focusing tends to blur the edges as well as the image making edge detection a difficult operation. All rebars and checkerboard boxes should be properly focused otherwise edge detection operation is affected. Poor focusing affects 2D and 3D part of algorithm during Hough transformation as well as extrinsic matrix computation from corners on checkerboard.

Detected Lines play a pivotal part in the algorithm and they depend upon edge detected binary image. Edges cannot be detected in an image if significant amount of blurring is present and thus Hough transform wouldn’t work.

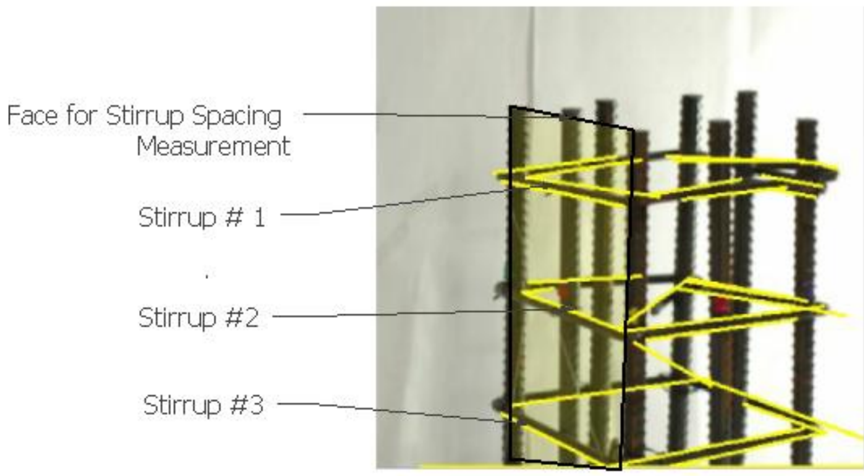

Figure 4.13 Well focused image with detected and extended lines

Figure 4.13 shows comparison of plotted Detected Lines on image that is well focused. As seen in the well-focused image on the right, the detected lines are drawn all around the stirrups very clearly. This will affect rebar width spacing measurement negatively, since the stirrup spacing is measured on the left face of the column as shown in **Figure 4.13** which shows image with poorly focused Detected Line on the stirrup measurement face.

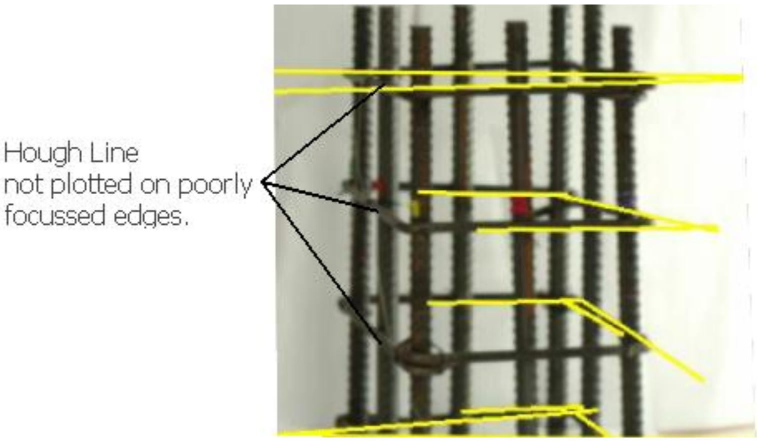

Figure 4.14 Detected Line on Poorly focused Image

As seen in Figure 4.14, the Detected Lines on stirrup measurement face are not clearly visible due to poor focusing. This has resulted in absence of Hough plot along stirrup measurement, therefore, giving no measurement for stirrup spacing in the poorly focused image. Error in stirrup spacing measured from Detected Lines shown in Figure 4.13 are represented by Figure 4.15.

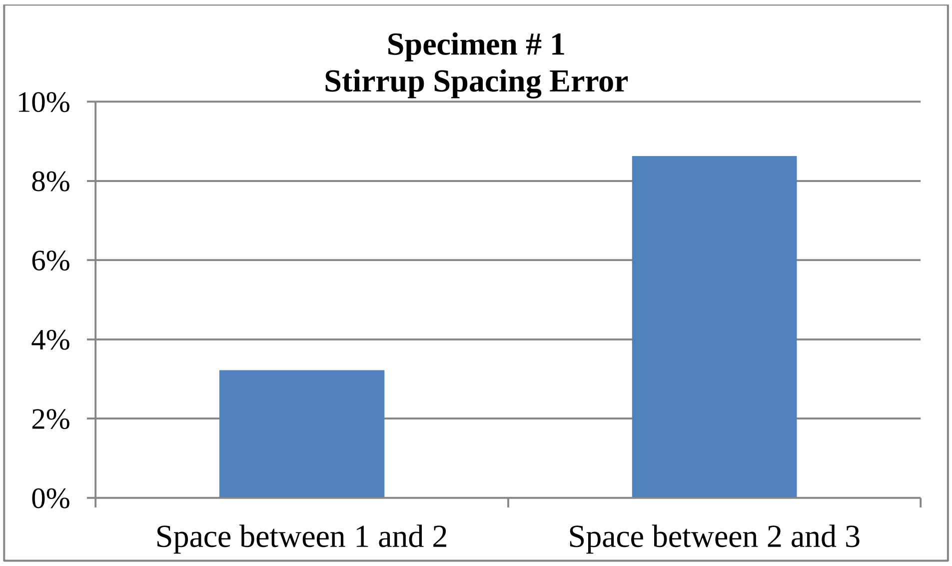

Figure 4.15 Graph representing error in Stirrup Spacing for Specimen # 1.

The error is reduced if same edge of both stirrups is detected while error is increased if opposite end of both stirrups is detected. E.g. in Figure 4.13, the top edge of stirrup 2 is detected while bottom edge in stirrup 3 is detected. The error would have been less if either top edges or both bottom edges of stirrup 2 and 3 were detected. Also the edges are not precisely detected and are offset from the real edge due to effect of blurring and Gaussian averaging performed on the image. For stirrup 1 both top edge and bottom edge are detected, while for stirrup, only top edge is detected. The algorithm measures distance between both of these top edges, therefore, providing less error. Here, it is also shown that, as measurement is done far from the checkerboard, the error is increased.

Figure 4.16 represents Detected Line plot on the image of Specimen # 2, The face perpendicular and nearest to the checkerboard is used for measurement of spacing between the Detected Lines. The image in Figure 4.16 is cropped for better representation.

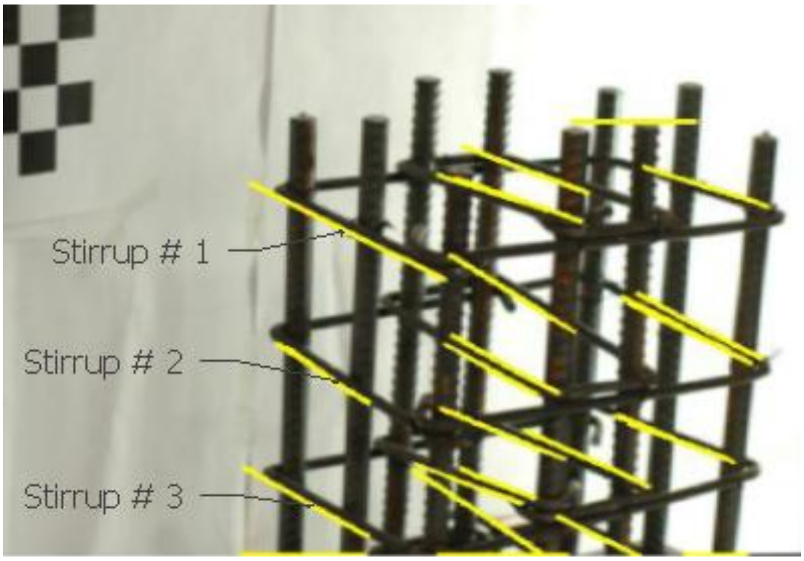

Figure 4.16 Specimen # 2 Image for Stirrup Spacing Measurement.

The pixels are counted between stirrups to measure the width. Figure 4.17 represents error in measurement between Stirrups shown in Figure 4.16. The resultant error increases as the stirrups are farther away from checkerboard. Since Detected Lines are on the same side of stirrups for all the stirrups, the error is considerably less as compared to error in Specimen # 1 represented in Figure 4.15

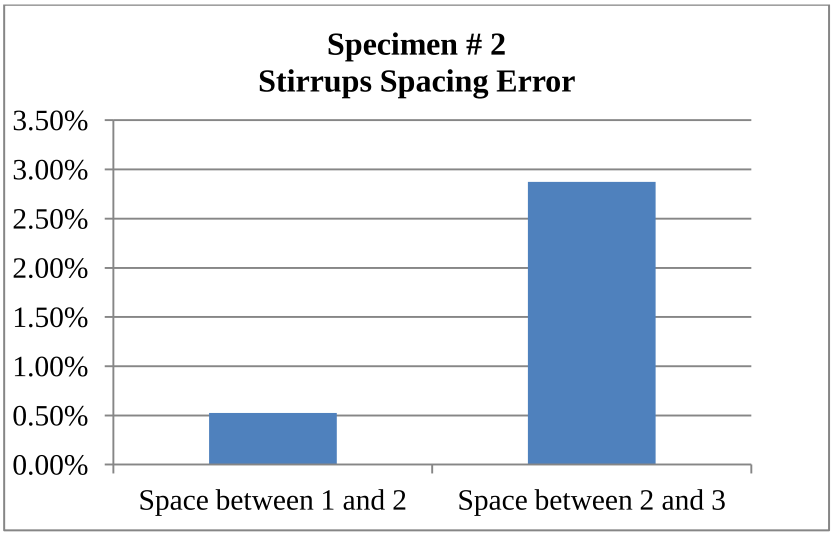

Figure 4.17 Graph representing error in Stirrup Spacing for Specimen # 2

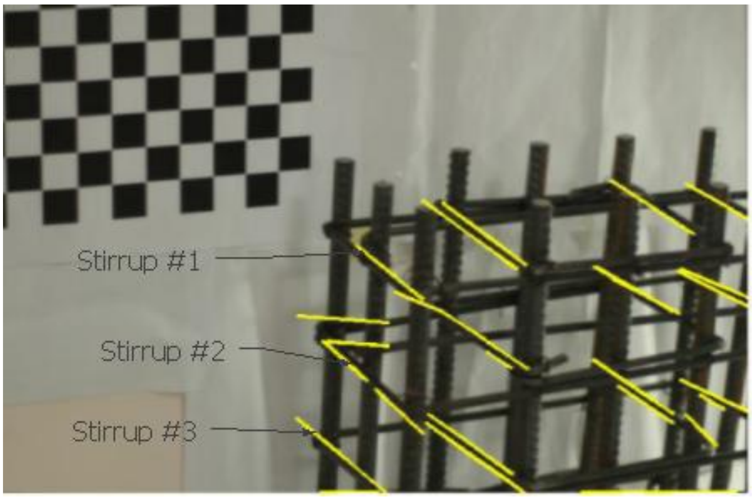

Figure 4.18 Specimen #3 Image for Stirrup Spacing Measurement

Figure 4.18 shows image of rebar taken with Detected Lines representing rebars. The distance between rebars would provide stirrup spacing. However, due to large number of internal and external stirrups, the detected lines don't lie exactly on the edge and are not parallel to the edge as well. The error in measurement of stirrup spacing is represented by bar plot in Figure 4.19.

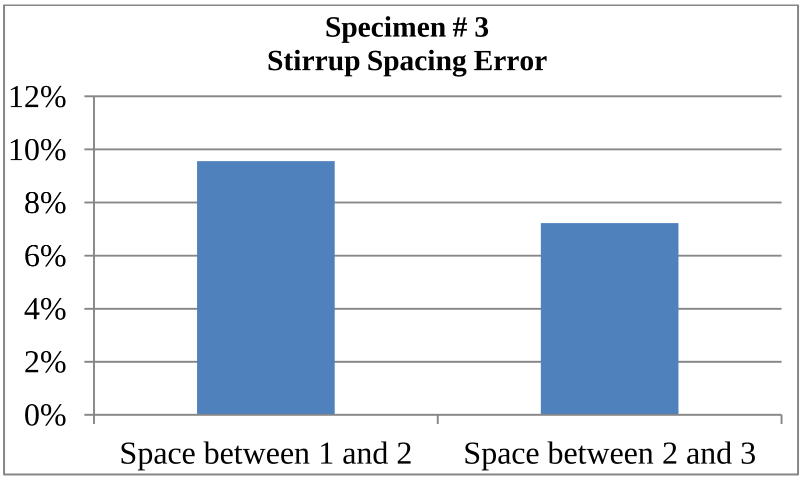

Figure 4.19 Errors in Stirrup Spacing Measurement in Specimen # 3.

The observation for Specimen # 3 is different than for other specimens since error is actually reducing as the stirrup moves away from the checkerboard. But this difference is due to cluttering and inability of the algorithm to exactly determine stirrup edges due to presence of rebars in going across the stirrups and the internal stirrups that are also seen in the image. Figure 4.20 represents error in stirrup spacing measurement.

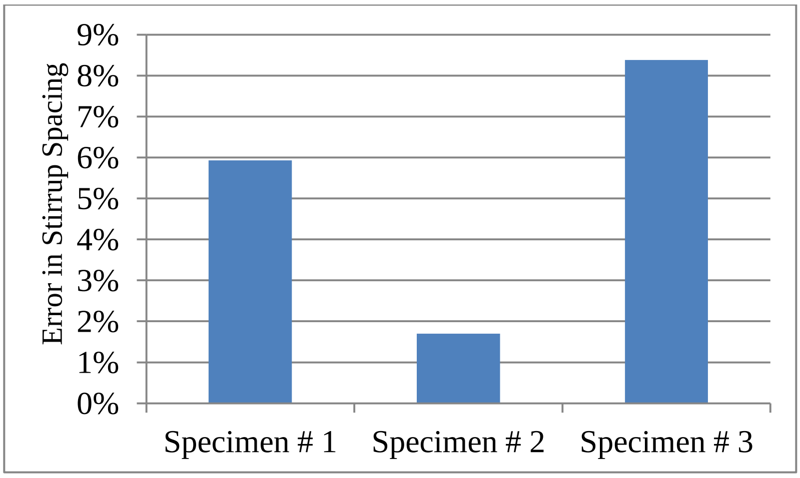

Figure 4.20 Average error in Stirrup Spacing Measurement for each Specimen

It is observed and seen from the error plot that error in stirrup spacing dependents upon the quality of Hough transform as well as quality of image and the amount of rebar density.

The error can be decreased by taking clearer images and avoiding sharp angles. Once the rebars are well focused with sharp edges, the Hough transform would be near the rebar edges thus giving good results. The checkerboard shouldn't be placed very far from the specimen as well.

4.6. Stereo Matching,

The specimen is hollow from inside and contains a large number of edges that appear as corners in the image. The results from the equation of fundamental matrix are not reliable because bars overlap each other, same pixel in one image may correspond to 2 different pixels in the stereo pair resulting in inaccurate output of stereo matching algorithm. The Detected Lines don't fall on the same edge of rebar in both images, which creates an error while the best match is being evaluated using functional matrix. This issue combined with overlapping of bars with each other provides false results that need further work to provide robustness. The algorithm will not work at all where there is cluttering of bars over each other. Stereo Matching was applied to

Specimen # 1 to determine the working of the algorithm and the number of correct matches achieved. The correctness of matches can be judged visually.

Figure 4.21 shows correct stereo matching of point 3 shown with an arrow in both stereo images. This is a representation of correct match. The numbers in Figure 4.21 are candidate for match. The candidate giving best value according to fundamental matrix equation is chosen to be the best match.

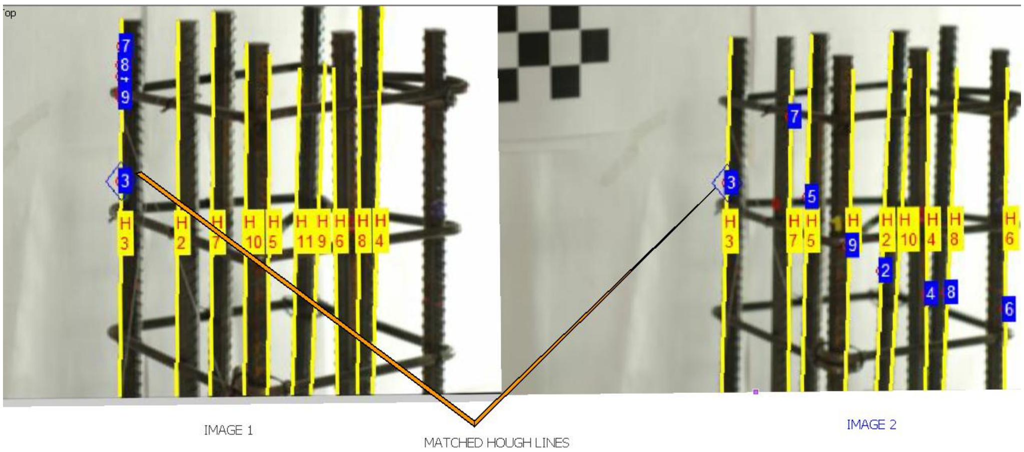

Figure 4.21 Pair of Stereo Image with Correct Matching.

The stereo matching algorithm is run for all rebar elements detected by Hough. The match of each Detected Line in image 1 is determined in image 2. There are 10 Detected Lines in Image 1, Detected Line 1 falls at the boundary of the image and is therefore ignored. Detected Line number contains H in the beginning, in order to differentiate the detected lines from matching points. 10 lines were correctly determined while Detected Line No. 4 in image 1 of **Figure 4.21** was matched with Detected Line No. 4 of image 2 instead of Detected Line No. 8 of Image 2.

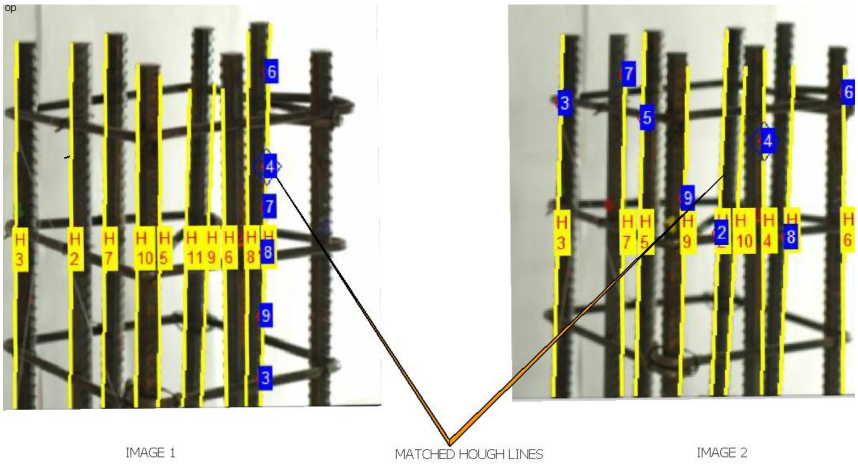

Figure 4.22 Wrongly Matched Detected Lines.

This is because of very close proximity of both Detected Lines and error in computation. The decision value obtained from Fundamental matrix equation matches Detected Line No. 4 of Image 1 to the wrong Detected Line in Image 2.

The stereo Matching algorithm was applied to Specimen # 2 as well. Figure 4.23 provides representation of correct stereo match in Specimen # 3.

Figure 4.23 Stereo Matching for Specimen # 3

Since the number of rebars overlapping each other is far greater for Specimen # 3 as compared to specimen #2, therefore the stereo matches are less reliable for Specimen #2 as compared to Specimen # 3. Out of 13 Detected Lines, there was only one correct match for Specimen # 3. The major reason for mismatch remains the overlapping of rebars. At times the lines are detected on different ends of rebar, thus inducing error in computation.

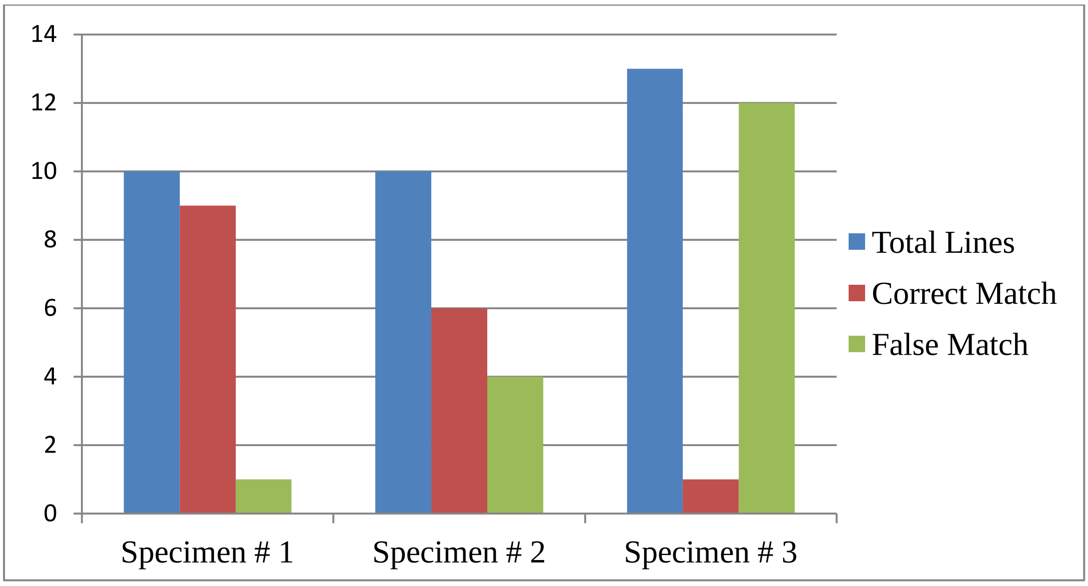

Figure 4.24 Number of Correct and False Stereo Matches for each Specimen.

Figure **4.24** provides the number of correct and false stereo matches for each specimen. It is observed that, as the number of rebars is increased and there are more occlusions, stereo matching becomes more and more inaccurate.

4.7. Error in Computation

Figure 4.25 shows representation of computed coordinates and actual location of rebars. 3D coordinate computation is based on manual matching of points on both images for greater accuracy. As seen in the Figure 4.25, error doesn't exceed 5 mm in both directions. The error is partly due to improper matching of stereo points but can be safely used in structural strength measurement computation and will provide realistic results.

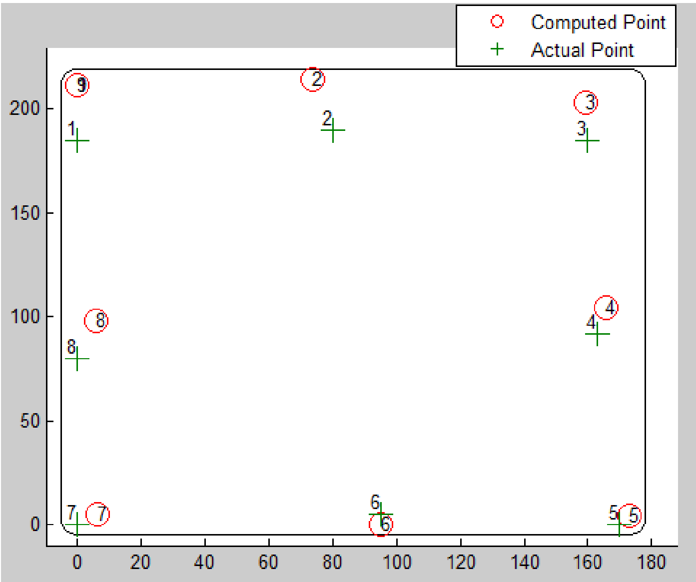

Figure 4.25 Rebar Coordinates determination for Specimen # 1.

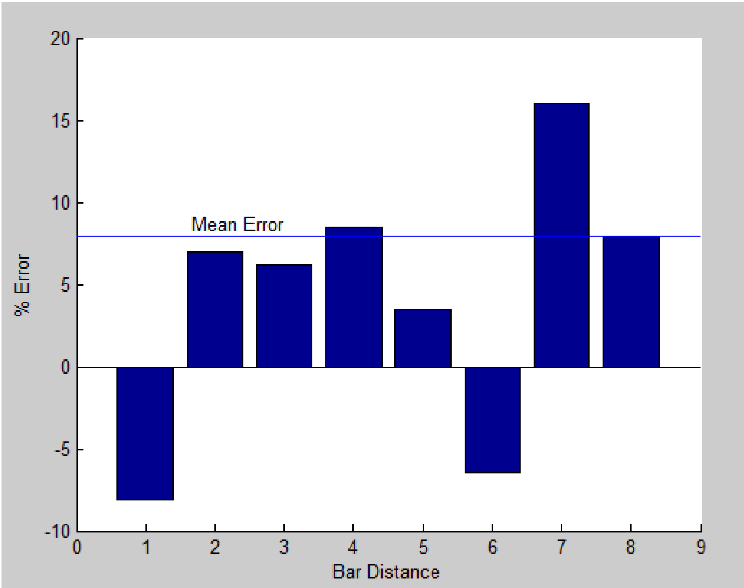

Figure 4.26 Percentage Error in Bar Width Spacing.

Figure 4.26 provides plot for bar spacing error between actual and computed rebar coordinates of Specimen # 2. As seen in Figure 4.26, the average error is 7% if we consider absolute values of all computation errors. The error in rebars on the farther end is greater than those near the grid. Figure 4.27 provides computed and actual location of rebar for Specimen #2. The error in bar spacing for the same Specimen # 2 is given in Figure 4.28.

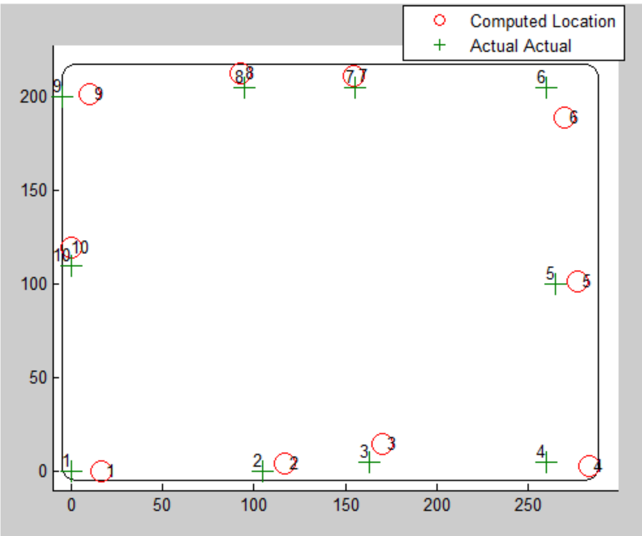

Figure 4.27 Computed and Actual Location Plot of Specimen # 2

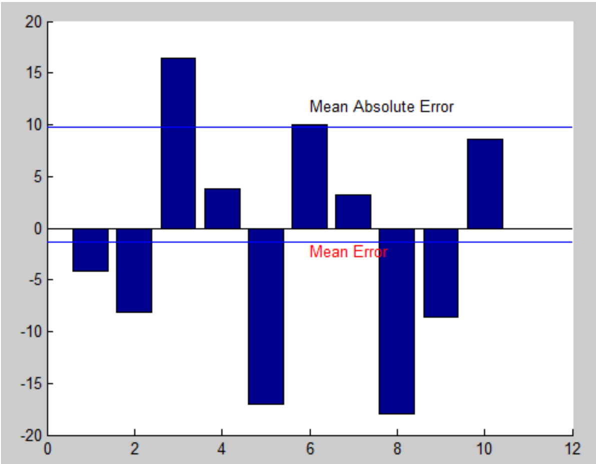

Figure 4.28 Error Plot for bar spacing of Specimen # 2.

As seen from the error plot and bar spacing plot, correct shape has been depicted and for 50% of the rebars, error is 5%. The error is due to difference in stereo matching points as well as error in calibration and imperfection in the Specimen. The cross section of the Specimen is not constant due to workmanship errors as well.

Specimen # 3 has also been plotted in following the 3D coordinate determination algorithm. Error in Specimen # 3 is very similar to error in Specimen # 1 and 2. Since the rebar coordinates are determined by manually matching points on the pair of stereo images, the effect of stereo matching doesn't appear. Figure 4.29 provides plot for actual and computed coordinates of rebar for Specimen # 3.

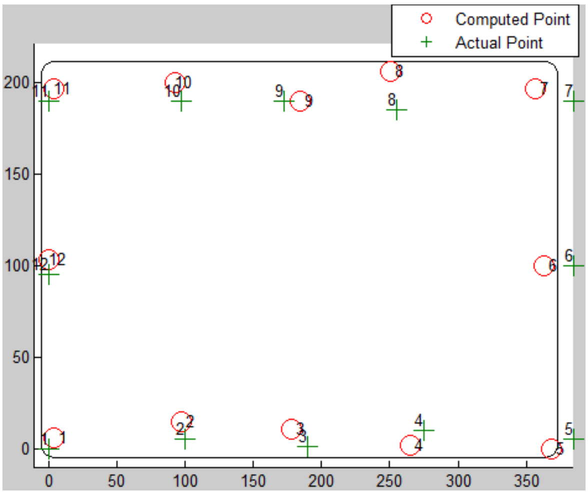

Figure 4.29 Actual vs. Computed Point plot for Specimen # 3

If we plot the error for bar spacing, the error is similar to specimen #1 and specimen # 2. The maximum error in longitudinal rebar spacing is 20% while mean average error is 9%. Figure 4.30 shows error plot for longitudinal rebar spacing and the error in computed spacing.

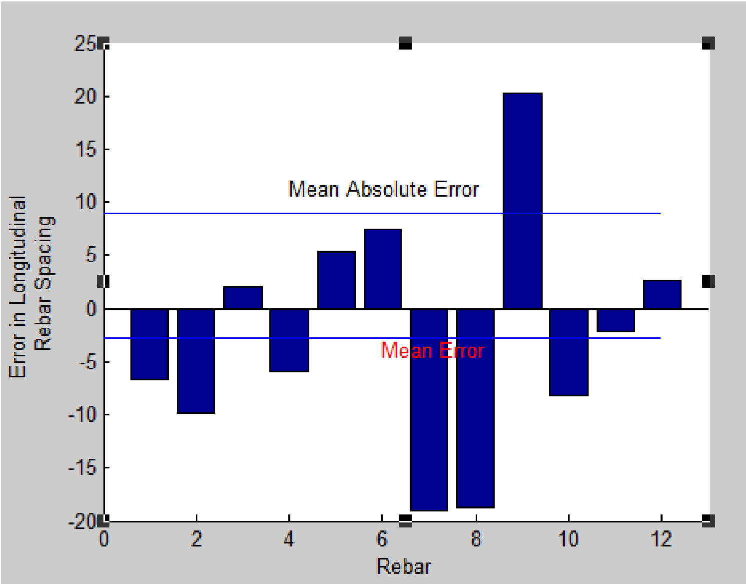

Figure 4.30 Bar Spacing Error Plot for Specimen # 3.

4.8. Scale Constraint

Greater the distance of object from the camera, greater is the error since, with the increase in distance, the width of pixel in millimeter increases and deviation of 1 x pixel width varies the result. The maximum allowable distance for triangulation is given by

$$d_{max} = \sigma_c \mathrm{c} \frac{\sqrt{k}}{q\sigma}$$

In order to test the scale constraint parameter, the object will be photographed from different distances. This parameter is related to computer vision part of the algorithm, therefore, all other elements including the bar specimen will be kept constant. The experiment would be done on specimen 1 and the sequence of image would be as follows

Table 4.3 Images and Distance of Image Acquisition

IMAGE	DISTANCE FROM SENSOR
1	1.3 m
2	2.5 m
3	3.7 m

The accuracy at different distances is measured and compared. The measurement would be done manually in order to achieve correct results.

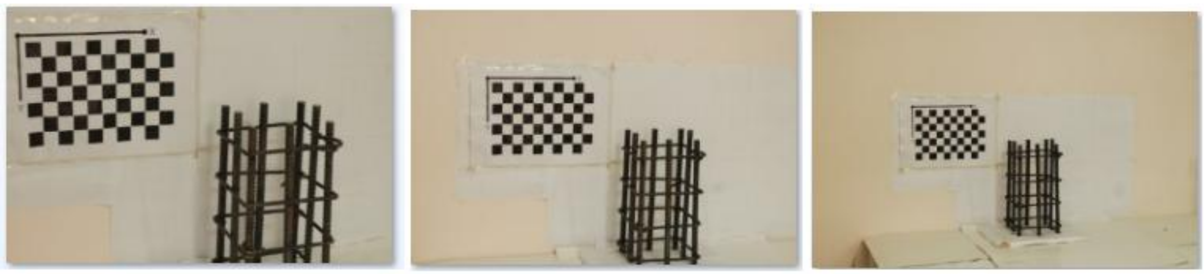

Figure 4.31 Image Acquisition at 1.3 m (Left), 2.5m (Center), 3.7m (Right).

Light, background, amount of noise and specimen are kept constant during the testing of parameters. The threshold for image processing part will also be kept constant.

Image was taken at distances mentioned in Table 4.3. As distance of image acquisition increases, the number of mm per pixel also increases. A wrongly selected pixel will cause greater error than the image taken at close distance. When imaging is done from a greater distance, the edges also become more blurred making it difficult to detect edges and resulting in Detected Lines that don't detect both edges of the rebars.

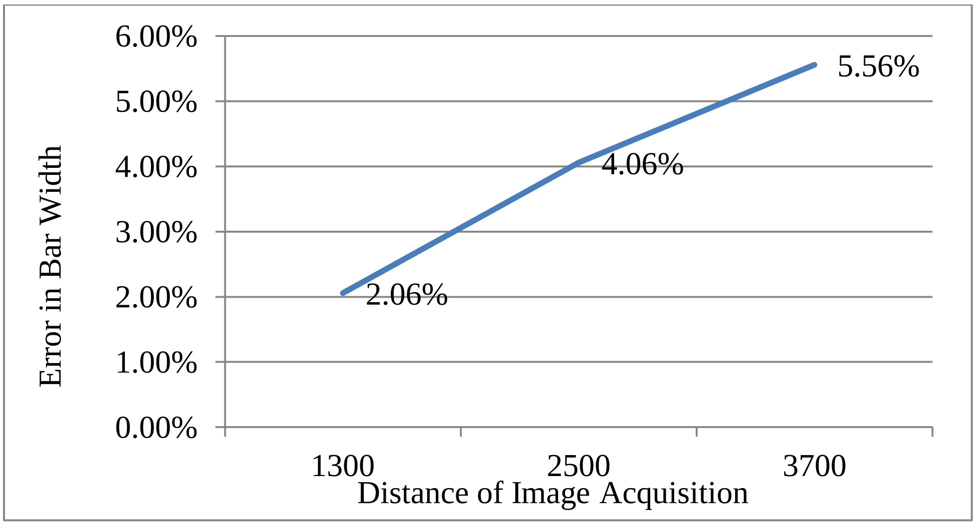

Figure 4.32 Error vs. Image distance graph.

4.9. Noise

Noise arises during image acquisition or transmission and is caused by image sensor or temperature conditions. Different types of noises are discussed in the literature that includes Gaussian, Salt and Pepper, Impulse Noise etc.

One image will be taken in good lighting conditions at a distance of 1.5m from the specimen B. Gaussian noise with different standard deviation values will be added to the same image and results will be compared.

The noise parameter affects only the image processing part of the algorithm, therefore, only measurement aspect is tested.

Table 4.4 Gaussian Variance used for different images

IMAGE No.	Gaussian Noise Variance
1	.01
2	.03
3	.05
4	.07

Only one image in daytime lighting and plain background in studio environment will be used. The image will be converted into binary image using the appropriate threshold values. The constants will not be changed during the course of evaluation and effect will be measured on 2D measurement only by manual measurement across the pixels.

Noise was added to images manually and bar width was determined using Hough transform. The width measurement for 18mm bars is shown in Figure 4.33, If Hough transform lines area is not detecting both ends of the bars, the number of pixels along the width of bars is manually checked and measurement is noted.

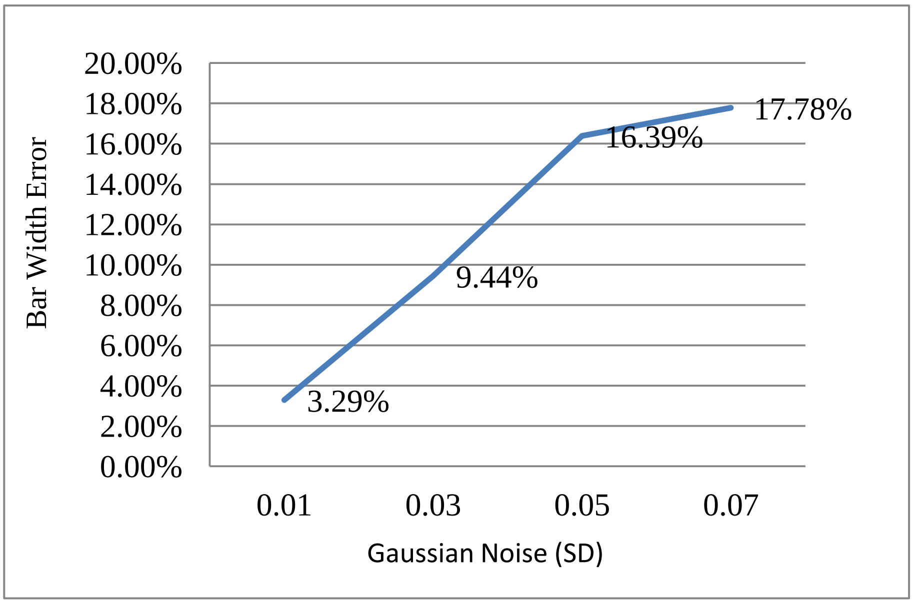

Figure 4.33 Bar width Error for image with different noise values.

4.10. Lighting Conditions

Light is an important parameter that can affect the results of algorithm. Dim light tends to ruin the quality of image and requires additional processing. Strong light from one end creates shadows which tend to create a false impression of elements which appear thicker than what they actually are and also creates an impression of bars number, greater than what are actually present. Since the bars are actually measured in 2D, the shadow of bar is considered similar to a bar. Light measurement was done using light meter tool for android that measures light incident on sensor based on exposure and F-Stop values. The interface for light measurement tool is given **in Figure 4.34**.

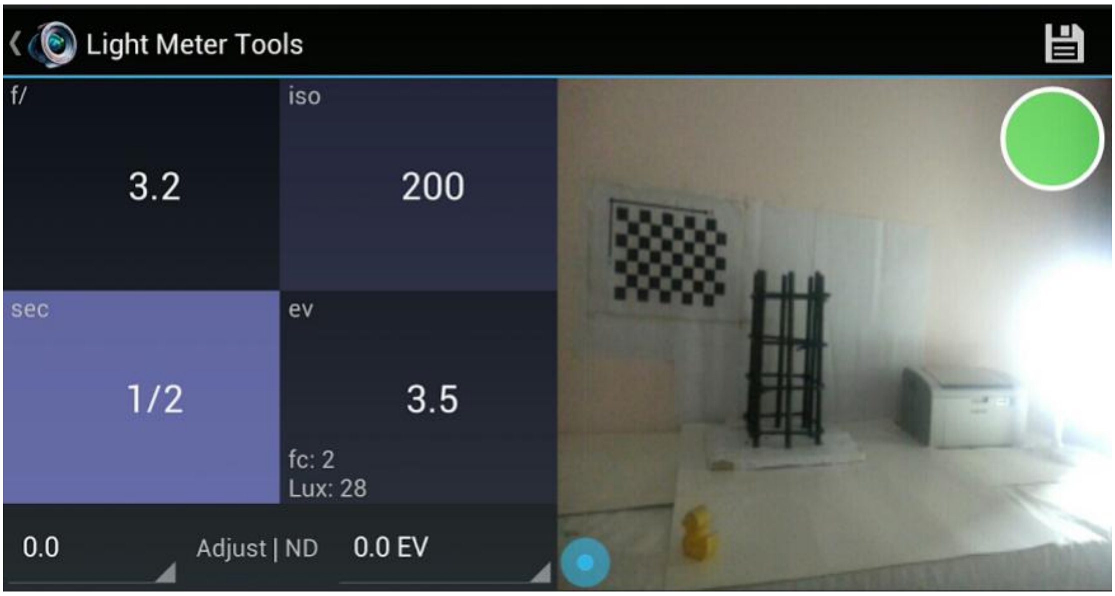

Figure 4.34 Light Measurement App interface.

The setup for measurement of bars includes taking pictures in varying lighting conditions. The algorithm will be run on varying lighting conditions, while keeping all other factors constant. The image will be taken at different times.

Table 4.5 Lighting Parameters

IMAGE No.	LUX
1	17
2	45
3	150

Lighting parameter is related to the image processing part of the algorithm, and in order to evaluate the parameter without the effect of algorithm, the measurement would be done manually. The final result would give the accuracy of 3D measurement. Figure 4.35 shows images taken in different lighting conditions.

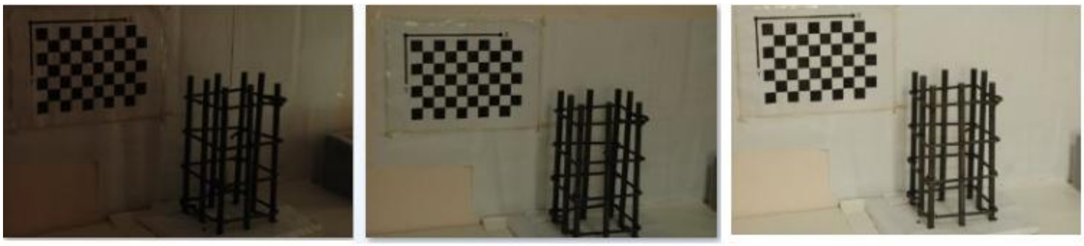

Figure 4.35 Imaging at 11 Lux (Left), 45 Lux (Center) and 150 Lux (Right)

Measurement was done in varying lighting conditions to determine the effect on width measurement rebars. The error of rebar diameter measurement in image 1, Image 2 and Image 3 is acquired in differing lighting conditions as shown in Figure 4.36, As clearly visible ,the error is high when lighting is very dim, the scene is dark and the edges are not easily differentiable.

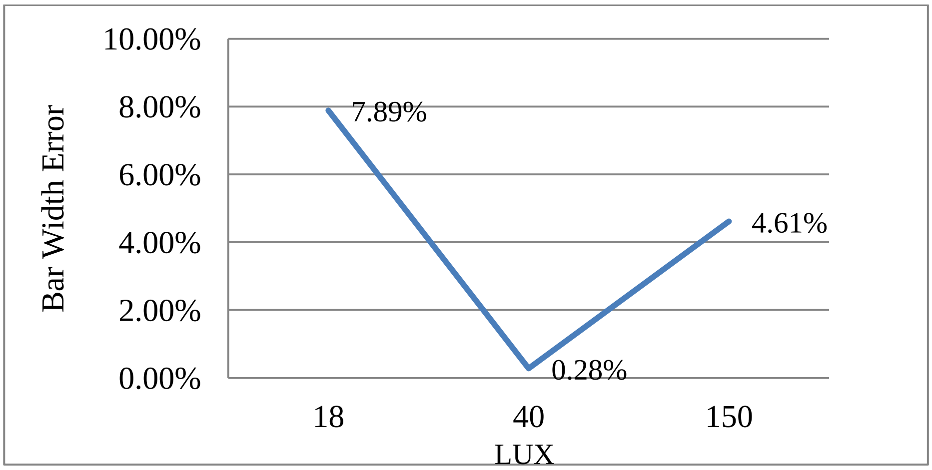

Figure 4.36 Bar Width vs. Lux Chart for image processing part

For very bright lighting, the error is increased again, since the edges become less visible in bright lighting conditions. The best results are obtained in lighting around 45-60 lux for such an experiment. The F-Stop was fixed at F3.2 and exposure was fixed at 1/50 sec in order to limit the exposure on sensor

Each algorithm of the method has been discussed in detail including results for the specimen prepared to test the algorithm. It has been observed that for the bar detection and measurement part of the algorithm, the results for all specimen are similar. The main difference appears during the 3D measurement part. The results for Specimen # 1 and Specimen # 2 are similar; however, the results for specimen # 3 show greater error. The conclusion being occlusion and cluttering of rebars in Specimen # 3 causes the major amount of errors.

CHAPTER 5

CONCLUSIONS

A study has been conducted on image processing and computer vision techniques in order to attain structural measurement information from images. Method involves acquisition of knowledge related to photogrammetry, image processing, computer vision, statistical analysis as well as mathematical modeling. In order to make the algorithm robust, multiple techniques including thresholding and Hough transformation have been applied. The problem at hand was multi-faceted because of requirement of measurement in both 2D and 3D domains. The measurement accuracy requirement for bar width is 1 mm; otherwise wrong bar width would be determined. The problem of occlusion is a big drawback that makes it difficult to create an automated and fully automatic mechanism to address the problem at hand. Multi prong approach was, therefore, applied to bring robustness through use of color space information as well as geometric Hough transformation based on orientation of edge elements. Once edges get blurred or are occluded behind each other, the quality of bar detection and bar width measurement is severely affected.
Three specimens constructed with different reinforcement details were tested to check the accuracy of the developed algorithm. For the square specimen with less number of longitudinal bars with respect to other specimens, errors in bar measurement and detection remained below 20%. As the specimen size increased and they became denser the accuracy of result was found to decrease.

The parametric testing has shown that lighting condition and distance of equipment from the object influence the results considerably. Threshold values are determined after evaluating 10 images acquired indoor under a combination of natural and artificial light. The manual threshold values need to be adjusted if image is acquired in completely artificial or natural lighting. The structural element for morphological operation is in the form of a line element which is 10 pixels long. The length of structural element needs to be modified in case the threshold values are not able to correctly find rebar pixels and there is presence of too many holes. Angle of imaging is also an important aspect; imaging from oblique angles would create issues in checkerboard detection and would give inaccurate results since checkerboard width would be distinctly different for all boxes making it difficult to detect boxes. Imaging from obtuse angle would not provide accurate reference width for measurement of bar width and stirrup spacing. The computation time is 5 minutes end to end.

The following specific conclusions are drawn from the study

a) The results are sensitive to image acquisition. Focusing and accurate acquisition of rebar grid and checkerboards will determine an accurate result.

b) Hough Transform for line detection detects only bar edges and cannot detect the center of rebars.

c) The developed method provides result with error less than 10% for bar detection on different specimen.

d) Error in Stirrup spacing measurement is less than 8.5% in controlled conditions. Error in stirrups closer to checkerboard is less than those stirrups farther away from checkerboard.

e) Error in rebar diameter measurement is 5.5% in controlled conditions for experiment done indoor in laboratory.

f) Maximum error in 3D rebar coordinate computation is 20% for spacing between rebars and absolute mean error is less than 10% for all specimens.

g) Stereo Matching is difficult problem to solve for rebar grids because of symmetry and hollow nature of rebars inside columns.

h) Error in 2D Measurement increase as distance from the column increases.

i) As Gaussian noise increase the error in 2D computation, the error also increases until Standard Deviation of noise is 0.05. Further increase in noise results in decrease of rate of error increase.

5.1. Rules for Image Acquisition

Images should be acquired in good lighting conditions while keeping the grid and the rebars in focus. Rebars from other columns shouldn't be visible through the specimen being imaged for application of method. Camera F-Stop and Aperture exposure shouldn't be altered during image acquisition. Lighting should be in a manner that no shadows appear behind the object. All kinds of image compression, sharpening and vibration reduction option built in the camera should be turned off. Only non-zoom lens should be used and calibrated for image acquisition. Imaging shouldn't be done in all artificial lighting and imaging should be done from an angle where there is minimum occlusion and overlapping of rebars.

Images should be acquired at different angles and background columns shouldn't be visible through the rebars. If background columns are visible through the column being photographed, line detection algorithm will detect false rebars and all rebar diameter as well as stirrup spacing algorithms results would be affected. Lighting should be arranged in a manner that there are no shadows appearing in the background of specimen. The edge detection algorithm will detect edges as rebar elements.

5.2. Opportunity for Future Research

Further work can be done in order to make the algorithm more robust and bring improvements to the stereo matching and bar detection parts of the algorithm. Requirement of line detection can be replaced with an alternative that doesn't rely on edge detection. Research can be done to further enhance the algorithm for application on beam, joint and shell elements as well as acquisition of information in IFC format for inter-operability.

REFERENCES

Abeid, J., Allouche, E., Arditi, D., & Hayman, M. (2003). PHOTO-NET II: a computer-based monitoring system applied to project management. *Automation in Construction*, *12*(5), 603–616.

Abudayyeh, O., Al Bataineh, M., & Abdel-Qader, I. (2004). An imaging data model for concrete bridge inspection. *Advances in Engineering Software*, *35*(8-9), 473–480.

Akinci, B., Boukamp, F., Gordon, C., Huber, D., Lyons, C., & Park, K. (2006). A formalism for utilization of sensor systems and integrated project models for active construction quality control. *Automation in Construction*, *15*(2),

Akinci, B., Fischer, M., Kunz, J., & Levitt, R. (2002). Representing Work Spaces Generically in Construction Method Models. *Journal of Construction Engineering and Management*, *128*(4), 296–305.

Ali Akbarnezhad, Ong, K. C. G., Chandra, L. R., & Lin, Z. (2012). Economic and Environmental Assessment of Deconstruction Strategies Using Building Information Modeling. In *Construction Research Congress* (pp. 1730–1739). West Lafayette, Indiana, United States: American Society of Civil Engineers.

Askey, P. (2004). NIKON D70 Review. *Digital Photography Review*. Retrieved Juy 06, 2014, from http://www.dpreview.com/reviews/nikond70/3

Authors, D., Bascle, B., Bernier, D, O., & Lemaire, D, V. (2006). A statistical approach for learning invariants: application to image color correction and learning invariants to illumination. In *ICONIP'06 Proceedings of the 13th international conference on Neural Information Processing* (pp. 294–303). Berlin: Springer-Verlag Berlin.

Bleyer, M., & Gelautz, M. (2007). Graph-cut-based stereo matching using image segmentation with symmetrical treatment of occlusions. *Signal Processing: Image Communication*, *22*(2), 127–143.

Bouguet, J.-Y. (2013). Camera Calibration Toolbox for Matlab. Retrieved July 06, 2014, from http://www.vision.caltech.edu/bouguetj/calib_doc/

Brilakis, I., Fathi, H., & Rashidi, A. (2011). Progressive 3D reconstruction of infrastructure with videogrammetry. *Automation in Construction*, *20*(7), 884–895.

Dimitrov, A., & Golparvar-Fard, M. (2014). Vision-based material recognition for automated monitoring of construction progress and generating building information modeling from unordered site image collections. *Advanced Engineering Informatics*, *28*(1), 37–49.

Eos Systems Inc. (2014). PhotoModeler Scanner. Retrieved July 06, 2014, from http://www.photomodeler.com/index.html

Fathi, H., & Brilakis, I. (2011). Automated sparse 3D point cloud generation of infrastructure using its distinctive visual features. *Advanced Engineering Informatics*, *25*(4), 760–770.

Fisher, R., Perkins, S., Walker, A., & Wolfart, E. (2003). Hough Transform. Retrieved July 06, 2014, from http://homepages.inf.ed.ac.uk/rbf/HIPR2/hough.htm

Fryer, J. . (2001). *Close Range Photogrammetry and Machine Vision*. (K. . Atkinson, Ed.) (2001st ed., p. 9). Bristol: J.W.Arrowsmith.

FUJIFILM Corporation. (2014). http://www.fujifilm.com/products/3d/camera/. Retrieved July 06, 2014, from http://www.fujifilm.com/products/3d/camera/

Goldstein, M. (2009). Fujifilm FinePix Real 3D W1 Review. Retrieved July 06, 2014, from http://www.photographyblog.com/reviews/fujifilm_finepix_real_3d_w1_review

Gonzales, R. ., & Woods, R. . (2008). *Digital Image Processing* (3rd ed.). Prentice Hall.

Gordon, C., Boukamp, F., Huber, D., Latimer, E., Park, K., & Akinci, B. (2003). Combining Reality Capture Technologies for Construction Defect Detection: A Case Study. In *EIA9: E-Activities and Intelligent Support in Design and the Built Environment, 9th EuropIA International Conference*, (pp. 99–108). Istanbul.

Hart, P. E., & Dunda, R. O. (1972). Use of the Hough Transformation to Detect Lines and Curves in Pictures. *Communications ACM*, *15*(April 1971), 11–15.

Hartley, R., & Zisserman, A. (2004). *Multiple View Geometry in Computer Vision [Paperback]* (Second., p. 670). Cambridge University Press; 2 edition.

Klein, L., Li, N., & Becerik-Gerber, B. (2012). Imaged-based verification of as-built documentation of operational buildings. *Automation in Construction*, *21*, 161–171. doi:10.1016/j.autcon.2011.05.023

Kolmogorov, V., & Zabih, R. (2001). Computing Visual Correspondence with Occlusions via Graph Cuts. In *IEEE International Conference on Computer Vision, ICCV 2001.* (pp. 508–515). IEEE.

Lefèvre, S., Mercier, L., Tiberghien, V., & Vincent, N. (2002). Applied to Background Extraction in Outdoor Images. In *1st European conference on color in Graphics, Image and Vision* (pp. 363–367). Poieters: Society of Imaging Science and Technolgy.

Leite, F., Akcamete, A., Akinci, B., Atasoy, G., & Kiziltas, S. (2011). Analysis of modeling effort and impact of different levels of detail in building information models. *Automation in Construction*, *20*(5), 601–609.

Mass, H.-G., & Hampel, U. (2006). Photogrammetric Techniques in Civil Engineering Material Testing & Structure Monitoring. *Photgrammetric Engineering & Remote Sensing*, *72*, 39–45.

Mei, X., Sun, X., Dong, W., Wang, H., & Zhang, X. (2013). Segment-Tree Based Cost Aggregation for Stereo Matching. *2013 IEEE Conference on Computer Vision and Pattern Recognition*, 313–320.

Olsen, M. J., Kuester, F., Chang, B. J., & Hutchinson, T. C. (2010). Terrestrial Laser Scanning-Based Structural Damage Assessment. *Journal of Computing in Civil Engineering*, *24*(3), 264–272.

Roh, S., Aziz, Z., & Peña-Mora, F. (2011). An object-based 3D walk-through model for interior construction progress monitoring. *Automation in Construction*, *20*(1), 66–75.

Sezen, H., Whittaker, A. ., Elwood, K. ., & Mosalam, K. . (2003). Performance of reinforced concrete buildings during the August 17, 1999 Kocaeli, Turkey earthquake, and seismic design and construction practise in Turkey. *Engineering Structures*, *25*(1), 103–114.

Shih, N.-J., Wu, M.-C., & Kunz, J. (2004). *The Inspection of As-Built Construction Records by 3D Point Clouds* (p. 90). Retrieved from http://cife.stanford.edu/sites/default/files/WP090.pdf

Śluzek, A. (2010). Novel machine vision methods for outdoor and built environments. *Automation in Construction*, *19*(3), 291–301.

Sohn, H.-G., Lim, Y.-M., Yun, K.-H., & Kim, G.-H. (2005). Monitoring Crack Changes in Concrete Structures. *Computer-Aided Civil and Infrastructure Engineering*, *20*(1), 52–61.

Son, H., & Kim, C. (2010). 3D structural component recognition and modeling method using color and 3D data for construction progress monitoring. *Automation in Construction*, *19*(7), 844–854. doi:10.1016/j.autcon.2010.03.003

Wada, N., Kaneko, S., & Takeguchi, T. (2006). Using color reach histogram for object search in colour and/or depth scene. *Pattern Recognition*, *39*(5), 881–888.

Yoon, K., & Kweon, I. (2005). Locally Adaptive Support-Weight Approach for Visual Correspondence Search. In *IEEE Computer Society Conference on Computer Vision and Pattern Recognition, CVPR 2005* (pp. 924–931).

Zhang, Z., Deriche, R., Faugeras, O., & Luong, Q. T. (1994). A Robust Technique for Matching Two Uncalibrated Images Through the Recovery of the Unknown Epipolar Geometry. *Artificial Intelligence*, *78*(1), 87–119.